Available online at www.sciencedirect.com

ScienceDirect

Geochimica et Cosmochimica Acta 234 (2018) 50–69

Geochimica et Cosmochimica Acta

www.elsevier.com/locate/gca

Crystallization of the lunar magma ocean and the primordial mantle-crust differentiation of the Moon

Bernard Charlier [a,b,c,*], Timothy L. Grove [a], Olivier Namur [b,d], Francois Holtz [b]

[a] Massachusetts Institute of Technology, Department of Earth, Atmospheric, and Planetary Sciences, Cambridge, MA 02139, USA
[b] Institut für Mineralogie, Leibniz Universität Hannover, 30167 Hannover, Germany
[c] Department of Geology, University of Liège, 4000 Sart Tilman, Belgium
[d] Department of Earth and Environmental Sciences, KU Leuven, 3000 Leuven, Belgium

Received 16 October 2017; accepted in revised form 4 May 2018;

Abstract

We present crystallization experiments on silicate melt compositions related to the lunar magma ocean (LMO) and its evolution with cooling. Our approach aims at constraining the primordial internal differentiation of the Moon into mantle and crust. We used graphite capsules in piston cylinder (1.35–0.80 GPa) and internally-heated pressure vessels (<0.50 GPa), over 1580–1020 °C, and produced melt compositions using a stepwise approach that reproduces fractional crystallization. Using our new experimental dataset, we define phase equilibria and equations predicting the saturation of liquidus phases, magma temperature, and crystal/melt partitioning for major elements relevant for the crystallization of the LMO. These empirical expressions are then used in a forward model that predicts the liquid line of descent and crystallization products of a 600 km-thick magma ocean. Our results show that the effects of changes in the bulk composition on the sequence of crystallization are minor. Our experiments also show the crystallization of a silica phase at ca. 1080 °C and we suggest that this phase might have contributed to the building of the lower anorthositic crust. Calculation of crustal thickness clearly shows that a thin crust similar to that revealed by GRAIL cannot have been generated through solidification of whole Moon magma ocean. We discuss the role of magma ocean depth, trapped liquid fraction (with implication for the alumina budget in the mantle and the crust), and the efficiency of plagioclase flotation in producing the thin crust. We also constrain the potential range of pyroxene compositions that could be incorporated into the crust and show that delayed crustal building during ca. 4% LMO crystallization on the nearside of the Moon may explain the dichotomy for Mg-number. Finally, we show that the LMO can produce magnesian anorthosites during the first stages of plagioclase crystallization.

Keywords: Lunar crust; Anorthosite; Mantle; Experimental petrology; Phase equilibria; Liquid line of descent

1. INTRODUCTION

The origin of the Moon has been generally attributed to a giant impact between a planet and the proto-Earth that ejected into orbit material from which the Moon accreted (Hartmann and Davis, 1975; Stevenson, 1987; Cameron and Benz, 1991; Canup and Asphaug, 2001; Canup, 2012; Ćuk and Stewart, 2012). Energy liberated in the giant impact event was sufficient to produce melting of a substantial portion of the Moon, a likely cause of a "Lunar Magma Ocean" (LMO; e.g. Tonks and Melosh, 1993; Elkins-Tanton, 2012). The LMO developed early between 4.5 and 4.3 Ga though the time of its initiation and its exact duration remains controversial (Kleine et al., 2005; Nemchin et al., 2009; Taylor et al., 2009; Touboul et al.,

* Corresponding author at: Department of Geology, University of Liege, 4000 Sart Tilman, Belgium.
E-mail address: b.charlier@uliege.be (B. Charlier).

https://doi.org/10.1016/j.gca.2018.05.006
0016-7037/

2009; Elkins-Tanton et al., 2011; Gaffney and Borg, 2014). Its crystallization appears to have structured the Moon into a mantle and a crust (e.g. Smith et al., 1970; Wood et al., 1970; Warren, 1985). However, direct evidence on how the LMO evolved chemically and physically as it cooled and crystallized remains a major issue. Petrologic models for the solidification of the LMO have been derived mainly from thermodynamic phase relationships assuming either fractional or equilibrium crystallization or some combination of the two (Longhi, 1977, 1980; Snyder et al., 1992; Elkins-Tanton et al., 2011). A recent study has experimentally constrained the early cumulate mineralogy in the solidified magma ocean (Elardo et al., 2011). The role of water during crystallization of the lunar magma ocean has been invoked (Lin et al., 2016, 2017), although volatile depletion of the Moon compared to Earth is still a matter of debate (Sharp et al., 2010; Elkins-Tanton and Grove, 2011; Canup et al., 2015).

The original and canonical model for LMO solidification involves plagioclase flotation to the top of a denser LMO and formation of a global anorthositic crust underlain by complementary mafic cumulates (Warren, 1985; Shearer et al., 2006). This model has been criticized and arguments invoked against this scenario are the young age of the anorthosite (Borg et al., 2011), the existence of magnesian anorthosites (Gross et al., 2014), and heterogeneity in plagioclase trace element concentrations (Russell et al., 2014) that are difficult to produce during magma ocean crystallization. A magma ocean also appears unable to produce noritic assemblages soon after plagioclase saturation because of early saturation with augite (Longhi, 2003).

However, alternative processes proposed for the formation of the anorthosite crust on the Moon do not necessarily invalidate the existence of an initial magma ocean, which would have produced the source rocks for the production of anorthosite by remelting and serial magmatism (Longhi, 2003; Gross et al., 2014; Longhi and Ashwal, 1985). Primordial differentiation of the Moon during magma ocean crystallization is still largely accepted to have produced deep cumulate rocks forming the lunar mantle, the source for surficial mare basalts (Snyder et al., 1992; Münker, 2010; Barr and Grove, 2013; Hui et al., 2013a; Hallis et al., 2014; Brown and Grove, 2015). Extreme differentiation of the LMO has also been suggested to lead eventually to the formation of urKREEP and titanium-rich cumulates (Longhi, 1977; Warren and Wasson, 1979b; Warren, 1985).

To place new constraints on the evolution of the LMO and its crystallization products, we have performed a series of crystallization experiments at 1.35–0.08 GPa and temperatures in the range 1580–1020 °C. These experimental results constrain the liquidus phase boundaries along the liquid line of descent of 600 km-thick lunar magma oceans with variable bulk compositions. Experiments are combined with numerical models using forward approaches of fractional crystallization. Our study brings new information on the amount of alumina stored in the mantle, the timing for the saturation of plagioclase, and the resulting crustal thickness that is produced by solidification of the LMO. We also discuss the origin of the nearside-farside dichotomy for the composition of pyroxene in the anorthositic crust and the formation of magnesian anorthosites. Primordial crust-mantle differentiation of the Moon is the main focus of this paper, with the objective to provide direct insights into the primary compositional stratification of the lunar interior. Defining the initial state of the Moon is essential to understand its subsequent evolution and specifically potential cumulate overturn, remelting, and production of mare basalts and ultramafic glasses (Solomon and Longhi, 1977; Hess and Parmentier, 1995; Elkins Tanton et al., 2002).

2. COMPOSITION AND DEPTH OF THE LUNAR MAGMA OCEAN

2.1. Bulk Moon compositions

The bulk composition of the silicate portion of the Moon has been estimated using various approaches and selected compositions are presented in Table 1. The main discriminating criterion among proposed compositions is the Mg-number (molar MgO/(MgO + FeO)) and a variation in the abundance of refractory elements (Ca, Al). This variability ranges from close to or greater than that inferred for Earth. Refractory lithophile elements are supposed to be in chondritic proportions with one another but their enrichment relative to CI chondrites and to Earth has been debated (e.g. Warren, 2005; Taylor et al., 2006). Estimates for the alumina content of the bulk Moon compositions mainly depend on the estimated thickness and composition of the crust. Both of these are not fully constrained values. The two end-member model compositions are: the Taylor Whole Moon model (TWM; Taylor and Bence, 1975; Taylor, 1982), which has an Al_2O_3 content that is 1.5 higher compared to Earth mantle, and the Lunar Primitive Upper Mantle model (LPUM; Jones and Delano, 1989; Longhi, 2003; Warren, 2005), which has an Al_2O_3 content that is similar to the terrestrial primitive upper mantle of Hart and Zindler (1986) with depletion of the alkali content. A third category represented by the compositions of O'Neill (1991) and Wänke and Dreibus (1982) has terrestrial refractory elements but a lower Mg-number.

More recently, isotopic studies have shown a high degree of similarity between Earth and Moon, which tends to support that lunar material was mainly derived from Earth (Wiechert et al., 2001; Touboul et al., 2007; Zhang et al., 2012; Dauphas et al., 2014). Impact simulations involving larger impactors support the possible formation of a disk of Earth-like composition (Canup, 2012). Additionally, recent data provided by the dual Gravity Recovery and Interior Laboratory (GRAIL) spacecraft have shown that the density of the Moon's crust is significantly lower than generally assumed (Wieczorek et al., 2013). Consequently, the average crustal thickness is suggested to be thinner, which implies that the bulk refractory element composition of the Moon (mainly Ca and Al) is not enriched with respect to that of Earth.

Although recent data tends to favor Earth-like concentrations for refractory elements in bulk Moon compositions

Table 1
Selected bulk silicate compositions of the Moon.

		SiO_2	TiO_2	Al_2O_3	Cr_2O_3	FeO	MnO	MgO	CaO	Na_2O	Sum	Mg#
Longhi (2006)	LPUM	46.10	0.17	3.93	0.50	7.62	0.13	38.30	3.18	0.05	99.98	0.90
Warren (2005)	W	46.80	0.18	3.87	0.44	9.24	0.13	36.00	3.06	0.05	99.77	0.87
Jones and Delano (1989)	JD	44.00	0.18	3.90		10.00	0.12	38.70	3.10		100.00	0.87
O'Neill (1991)	ON	44.60	0.17	3.90	0.47	12.40	0.17	35.10	3.30	0.05	100.16	0.83
Wänke and Dreibus (1982)	WD	44.30	0.18	3.76	0.37	12.65	0.16	35.50	3.15	0.06	100.13	0.83
Taylor (1982)	TWM	44.40	0.31	6.14	0.61	10.90	0.15	32.70	4.60	0.09	99.90	0.84
Taylor and Bence (1975)	TB	45.90	0.30	6.00		10.50		32.40	4.90	0.10	100.10	0.85

$K_2O = 0.01$; $P_2O_5 = 0.02$ wt% based on the composition of the bulk silicate Earth (McDonough and Sun, 1995).

(Taylor and Wieczorek, 2014), uncertainties about the bulk lunar Mg-number remain, as this parameter is sensitive to oxygen fugacity during the accretion of the Moon, and core formation of Earth and the Moon. Consequently, despite the constraints on the bulk Moon composition that have been provided by samples from both meteorites and samples returned by the Apollo and Luna missions, geophysical data, remote sensing, isotopic data, and hydrodynamic simulations, no clear consensus has yet arisen. In this study, the proposed range of potential compositions will be discussed although the discussions will focus on an alkali-depleted Earth-like lunar magma ocean. As we shall demonstrate this Earth-like bulk compositions satisfies the constraints we have from lunar crustal thickness and composition.

2.2. Depth of the magma ocean

The extent of initial lunar melting and the depth of the magma ocean has been estimated using various approaches but no definitive consensus has been reached (e.g. Solomon, 1980; Warren, 1985; Longhi, 2006; Rai and van Westrenen, 2014; Steenstra et al., 2016). Today, the accepted range varies from entirely molten Moon to shallow magma ocean (ca. 500–600 km thick; Fig. 1). In this study, experiments have been performed to simulate a magma ocean of 600 km depth. This choice is mainly based on the inability for an initially totally molten Moon to produce a thin crust

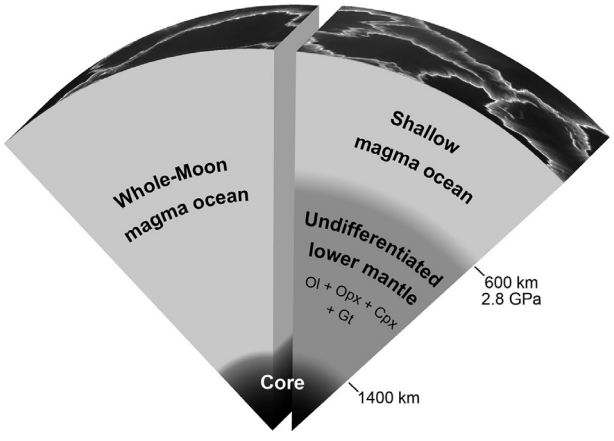

Fig. 1. Schematic diagram of the internal structure of the Moon illustrating the formation of a fully molten Moon vs. a shallow magma ocean on top of an undifferentiated lower mantle, assumed to have the same bulk composition as the magma ocean.

(Longhi, 2006), as revealed by recent GRAIL data (Wieczorek et al., 2013). Additional lines of evidence are detailed below.

Geophysical modelling converges upon the existence of major discontinuity in seismic velocity and density in the mantle at a depth of about 500–550 km (Nakamura, 1983; Hood and Jones, 1987; Khan et al., 2000, 2006; Lognonné, 2005). This discontinuity has been suggested to mark the lowest extent of early lunar differentiation, representing the limit between fractionated upper mantle and primordial lower mantle (Mueller et al., 1988). However, a broad range of acceptable models has been proposed and caution should be taken with the interpretation of that seismic discontinuity (Gagnepain-Beyneix et al., 2006; Wieczorek et al., 2006; Lognonné and Johnson, 2007; Khan et al., 2013). Recent extensional tectonics on the Moon may be inconsistent with a totally molten early Moon, and favor a partially molten Moon with the undifferentiated lower mantle being relatively close to the solidus (Solomon and Chaiken, 1976; Kirk and Stevenson, 1989; Watters et al., 2012).

Some studies have suggested the existence of garnet in the deep mantle that has been preserved from melting (Beard et al., 1998; Neal, 2001; Draper et al., 2006; Barr and Grove, 2013). Experiments by Elardo et al. (2011) have shown that garnet is not close to the liquidus of any bulk Moon compositions, meaning that whole Moon magma ocean would not produce garnet in a cumulate sequence formed by fractional crystallization. Consequently, the presence of garnet in the deep interior seems to imply a shallower magma ocean and an underlying undifferentiated garnet-bearing source.

3. FORWARD MODELLING OF DIFFERENTIATION

New experiments are used to constrain phase equilibria and crystal/liquid partitioning used in an incremental model of mass balance calculation between liquid and solid. Calculations are performed for each major element oxide (SiO_2, TiO_2, Al_2O_3, Cr_2O_3, FeO_{tot}, MnO, MgO, CaO, Na_2O, K_2O and P_2O_5). Fe_2O_3 being negligible at conditions of oxygen fugacity close and below the IW buffer relevant for the Moon (Sato et al., 1973), all the iron was considered as FeO.

Fractional crystallization can be modelled using the following equation:

$$c^{0}_{i,Liq} = (1 - z) * c^{l}_{i,Liq} + z * \left[\left(\sum_{j=1 \rightarrow n} X^{j} c^{j}_{i} \right) * X^{Mush}_{Sol} + c^{0}_{i,Liq} X^{Mush}_{Liq} \right]$$

where z is the sequential increment of crystallization (fixed here as 1% of the remaining liquid), $c^{l}_{i,Liq}$ is the concentration of element i in the liquid at each step of fractionation, $c^{0}_{i,Liq}$ is the concentration of element i in the liquid at the previous step of fractionation, c^{j}_{i} is the concentration of element *i* in crystalline phase j, X^{j} is the proportion of phase j in the cumulus assemblage, X^{Mush}_{Sol} is the bulk proportion of solid in the crystal + trapped liquid mush and X^{Mush}_{Liq} is the proportion of trapped liquid in the crystal + liquid mush.

The magma ocean is considered to crystallize bottom up (Walker et al., 1975; Warren and Wasson, 1979a; Elkins-Tanton, 2012) and to strongly convect so that there is no chemical gradient from the bottom to the top of the LMO. Our modelling strategy is inspired by the studies of Elkins-Tanton et al. (2003, 2011). As a first approach, the pressure at 600 km depth in the LMO has been calculated using a liquid density of 2.8 g cm^{-3}. The pressure has then been refined by taking into account the effect of pressure on liquid density, following the expression of Bottinga and Weill (1970) (see Supplementary Materials). This calculation method gives pressure of 2.79–2.86 GPa at 600 km (fraction of residual liquid F = 1), depending on the bulk Moon composition considered. The pressure decreases with crystallization, proportionally to the amount of subtracted cumulate in a sphere. The densities of solid phases are calculated at the solidus temperature and the effect of pressure on density is calculated for each phase using the Birch-Murnaghan equation of state (see Supplementary Materials). Using the masses of crystallized cumulates and their density enables the calculation of the cumulate thickness for each increment of crystallization and thus the depth of the residual LMO. In our model, we can assume that either plagioclase accumulates at the bottom of the LMO or floats to the top of the LMO. When flotation is taken into account, we can calculate a theoretical thickness for the anorthosite crust.

4. THE EARLY EVOLUTION OF THE LUNAR MAGMA OCEAN

For the Bulk Moon compositions olivine is the liquidus phase over the entire range of pressure relevant for the LMO (Longhi, 2006; Longhi et al., 2010; Elardo et al., 2011; Lin et al., 2016, 2017). The first steps of differentiation can thus be simply calculated by simulating crystallization of olivine (see Supplementary Material for details on the calculation of olivine compositions). Liquid compositional evolution for each bulk composition was tracked by removing olivine to the point of low-Ca pyroxene saturation at the appropriate depth (pressure) in the crystallizing LMO. This simple fractionation model enables us to test early compositional evolution of residual melts under conditions of fractional crystallization before orthopyroxene saturation, with variable proportions of trapped liquid in the subtracted olivine cumulate (dunite). Bulk Moon compositions and the liquid lines of descent produced by fractional crystallization of olivine with proportions of trapped liquid of 0, 5 and 10% are plotted in Fig. 2.

Trapped liquid has no effect on the liquid line of descent but influences the fraction of residual liquid (F) to be reached before attaining a given degree of liquid evolution (e.g. MgO content of the residual LMO). More trapped liquid results in a lower F, which thus influences the crystallization pressure. However, as illustrated in Fig. 2, this effect is minor and considered as secondary compared to the compositional range of bulk Moon composition that is investigated in this study. The residual compositions obtained after olivine subtraction (no trapped liquid) were selected as starting compositions for the experiments described below. They are illustrated in Fig. 2 and reported in Table 2.

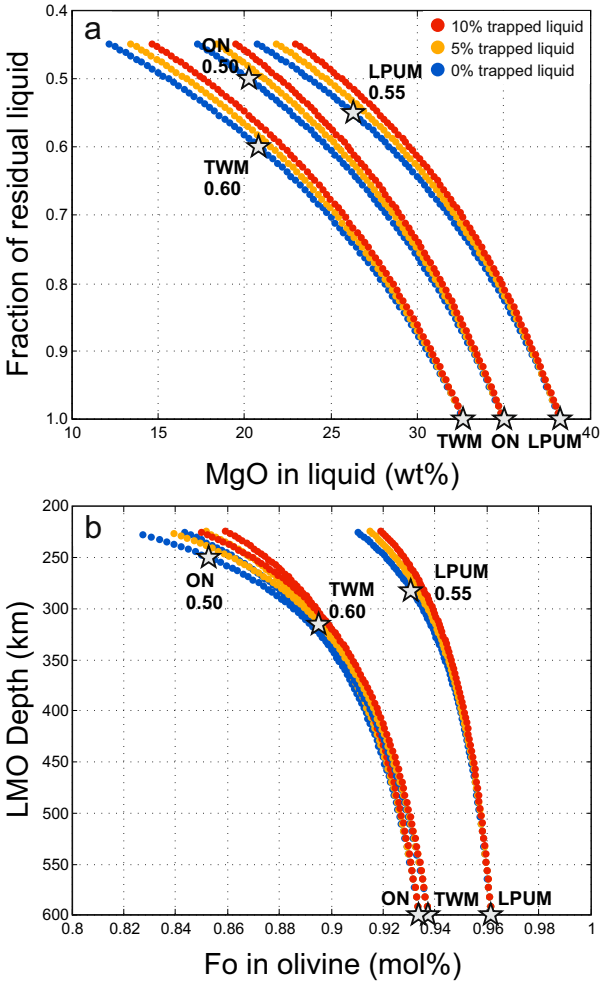

Fig. 2. Early chemical evolution of the lunar magma ocean during olivine fractionation, with 0, 5, and 10 wt.% trapped liquid in the subtracted olivine cumulate. (a) Fraction of residual liquids (wt.%) vs. MgO (wt.%) in the residual melts; (b) Depth (km) in the shallow lunar magma ocean (initial depth of 600 km) as a function of the forsterite content in olivine (mol%).

Table 2
Starting compositions, experimental methods and conditions.

	Pressure (GPa)	Temp (°C)	Method	SiO_2	TiO_2	Al_2O_3	Cr_2O_3	FeO	MnO	MgO	CaO	Na_2O	K_2O	P_2O_5	Sum
TB[a] (F = 0.60)	1.35	1500–1400	PC	48.66	0.50	9.97	0.51	12.18	0.15	19.70	8.15	0.17	0.02		100
JD[a] (F = 0.40)	0.85	1450–1300	PC	47.86	0.45	9.74	0.51	14.08	0.12	19.50	7.74				100
ON[a] (F = 0.50)	1.10	1530–1350	PC	48.34	0.34	7.82	0.47	15.92	0.17	20.21	6.62	0.10			100
ON[a] (F = 0.44)	0.95	1440–1360	PC	49.44	0.39	8.83	0.47	16.16	0.17	16.95	7.48	0.11			100
ON66	0.80	1380–1260	PC	47.50	0.50	11.00	0.40	17.30	0.15	13.60	9.40	0.15			100
ON66	0.50	1250–1210	IHPV	47.50	0.50	11.00	0.40	17.30	0.15	13.60	9.40	0.15			100
ON72	0.50	1250–1170	IHPV	46.32	0.64	14.09	0.17	17.96	0.17	8.39	12.08	0.17			100
ON72/05-5	0.30	1180–1130	IHPV	47.77	0.99	14.29	0.15	18.98	0.28	5.36	11.40	0.25	0.08		100
ON/02-3	0.15	1100–1040	IHPV	49.32	1.55	11.08	0.09	23.01	0.35	3.20	10.70	0.31	0.12	0.27	100
ON/04-1.5	0.08	1020	IHPV	47.54	2.59	8.57		28.17	0.43	1.29	10.32	0.36	0.24	0.49	100
TWM[a] (F = 0.60)	1.35	1500–1360	PC	46.85	0.52	10.30	0.62	12.92	0.15	20.76	7.72	0.15			100
TWM71	0.80	1380–1260	PC	45.82	0.72	13.53	0.33	13.99	0.13	14.73	10.49	0.25			100
TWM71	0.50	1250–1210	IHPV	45.82	0.72	13.53	0.33	13.99	0.13	14.73	10.49	0.25			100
TWM95	0.50	1250–1170	IHPV	47.50	0.82	15.39	0.25	13.05	0.13	10.47	12.17	0.21			100
TWM95/05-5	0.30	1180–1130	IHPV	47.00	2.19	13.14	0.12	20.24	0.20	5.28	11.65	0.24	0.08		100
TWM/02-3	0.15	1100–1040	IHPV	47.66	2.99	10.72	0.09	22.85	0.35	3.63	11.03	0.27	0.14	0.27	100
TWM/04-1.5	0.08	1020	IHPV	46.29	4.75	8.47		27.13	0.43	1.54	10.37	0.28	0.27	0.47	100
LPU[a]M (F = 0.55)	1.20	1580–1400	PC	49.88	0.31	7.14	0.51	9.78	0.13	26.39	5.78	0.09			100
LPUM88	0.50	1250–1210	IHPV	49.31	0.63	13.34	0.27	10.53	0.10	13.99	11.63	0.20			100
LPUM/02-5	0.30	1180–1130	IHPV	47.59	2.16	14.51	0.13	15.81	0.10	6.76	12.43	0.42	0.06		100
LPUM/02-3	0.15	1100–1040	IHPV	47.58	4.27	10.78	0.09	21.39	0.22	3.80	10.94	0.51	0.14	0.27	100
LPUM/04-1.5	0.08	1020	IHPV	48.09	4.19	8.67		25.65	0.28	1.61	10.11	0.56	0.29	0.55	100

PC = Piston Cylinder; IHPV = Internally heated pressure vessel.

[a] Calculated by subtracting olivine (fractional crystallization without trapped liquid) to the corresponding bulk silicate compositions of the Moon (Table 1).

In this study, we consider a 600 km-deep LMO. The depth of the LMO may influence its crystallization sequence because of the effect of pressure on phase boundaries (e.g. Warren and Wasson, 1979a). Increasing pressure enhances the stability field of orthopyroxene at the expense of olivine. Orthopyroxene will appear at higher temperature (more primitive compositions) in a deeper magma ocean and, after orthopyroxene saturation, the proportion of orthopyroxene in the orthopyroxene-olivine cotectic assemblage will be lower. Additionally, plagioclase stability is also affected by pressure so that a lower fraction of residual liquid is expected to be reached in a deeper magma ocean before the liquid line of descent enters the plagioclase crystallization field. However, we consider these effects do not have significant implications for the conclusions of this study because, as illustrated later, late-stage residual liquids all converge to the same restricted range of compositions.

5. EXPERIMENTAL AND ANALYTICAL METHODS

5.1. Experimental strategy

The experimental study aims at simulating the evolution of the lunar magma ocean during cooling, accumulation of crystallized material on the floor, and decreasing pressure with evolving residual liquid composition (Fig. 3; Table 2). The first stage of olivine crystallization was calculated and we selected five compositions to track orthopyroxene appearance as the starting point for this experimental study (Table 2 and Supplementary Table S1). We then produced melt compositions that have evolved by fractional crystallization using a stepwise experimental approach, by making up new starting materials having the composition of the residual melts after some degree of crystallization. Experiments on these new starting materials represent crystallization of evolving residual liquid composition and are performed at decreasing pressure, proportional to the fraction of crystallized minerals in the previous higher-temperature experiments. The main objective of the experimental investigation is to identify the position of phase boundaries in the appropriate compositional field and pressure range, and to build a consistent dataset to constrain crystal-liquid partitioning for major elements during LMO solidification.

We first performed a series of experiments on the early evolution of five bulk Moon compositions from which olivine has been subtracted: the TB composition (Taylor and Bence, 1975), the JD composition (Jones and Delano, 1989), the O'Neill bulk Moon composition (ON; O'Neill, 1991), the Taylor Whole Moon (TWM; Taylor, 1982), and the Lunar Primitive Upper Mantle (LPUM; Longhi, 2006) (Table 2). We then performed additional steps of crystallization at lower pressure on residual liquids from the ON, TWM, and LPUM compositions for which complete sequences of crystallization were obtained.

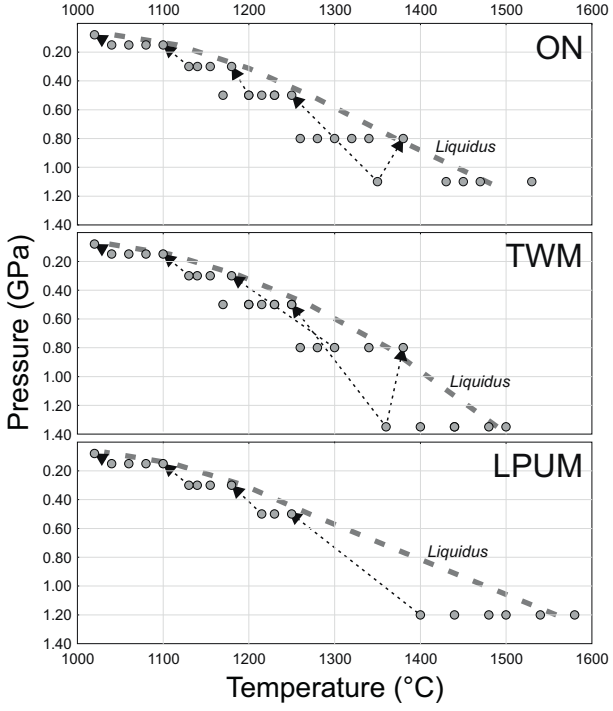

Fig. 3. Pressure and temperature conditions for individual experiments performed on residual melts from the O'Neill bulk Moon composition (ON), the Taylor Whole Moon composition (TWM), and the Lunar Primitive Upper Mantle composition (LPUM; see Table 1 for references). The liquidus curves were defined based on our new super-liquidus experiments and experiments with very low crystal fractions.

5.2. Starting materials and experimental techniques

Starting compositions were prepared by mixing high purity oxides and silicates. We used SiO_2, TiO_2, Al_2O_3, Cr_2O_3, MnO, MgO, $CaSiO_3$, Na_2SiO_3 and $K_2Si_4O_9$ in the appropriate proportions. Iron was added as Fe_2O_3 and Fe metal sponge in stoichiometric proportions to produce FeO. The reagents were mixed under ethanol in an agate mortar for 5 h. The Fe sponge was then added to the mixture and ground for an additional hour. The mixtures were then conditioned at 1-atm pressure in a DelTech vertical gas-mixing furnace for 24–48 h at oxygen fugacity corresponding to the Fe-FeO buffer at 1000 °C.

High-pressure experiments (≥0.80 GPa) were performed in piston-cylinder devices at MIT using a 0.5″ Boyd-England style end-loaded piston cylinder apparatus (Boyd and England, 1960) with the hot piston-in technique (Johannes et al., 1971). The starting material was packed into a graphite capsule and dried in a desiccated drying oven at 120 °C for >24 h. The capsule was surrounded by a dense Al_2O_3 sleeve and centered within a graphite furnace using crushable MgO spacers. The use of graphite capsule without outer Pt capsule resulted in contamination by Na (gain of 0.2 up to 2 wt.% Na_2O depending on the duration of the experiment). The use of an outer Pt capsule hampered any contamination. The addition of Na to the starting composition produces a lower quartz component and higher plagioclase and olivine components in the melt, potentially shifting the composition from the stability field of orthopyroxene to that of olivine. This is illustrated by experiments on the composition T&B0.6 (Table 3) which

Table 3
Experiments and run conditions.

Starting composition	Run	Pressure (GPa)	Temp (°C)	Duration (hrs)	Capsule	Phases	r^2
T&B (F = 0.60)	B1207	1.35	1500	6	C	gl (100)	–
T&B (F = 0.60)	B1213	1.35	1480	6	C	gl (94), opx (6)	0.01
T&B (F = 0.60)	B1211	1.35	1460	6	C	gl (93), ol (5), opx (2)	0.02
T&B (F = 0.60)	B1209	1.35	1400	22	C	gl (76), ol (10), opx (15)	0.00
T&B (F = 0.60)	B1261	1.35	1400	20	C + Pt	gl (76), opx (24)	0.07
T&B (F = 0.60)	B1258	1.35	1360	50	C + Pt	gl (57), opx (43)	1.15
ON (F = 0.50)	B1219	1.10	1530	5	C	gl (100)	–
ON (F = 0.50)	B1255	1.10	1470	6	C	gl (94), ol (6)	0.02
ON (F = 0.50)	B1242	1.10	1450	8	C	gl (86), ol (9), opx (5)	0.05
ON (F = 0.50)	B1254	1.10	1430	8	C	gl (81), ol (6), opx (13)	0.07
ON (F = 0.50)	**B1266**	**1.10**	**1350**	**48**	**C + Pt**	**gl (62), ol (8), opx (30)**	**0.17**
ON (F = 0.44)	B1238	0.95	1440	6	C	gl (100)	–
ON (F = 0.44)	B1239	0.95	1400	6	C	gl (98), opx (2)	0.05
ON (F = 0.44)	B1240	0.95	1360	6	C	gl (81), opx (19)	0.02
TWM (F = 0.60)	B1246	1.35	1500	4	C	gl (100)	–
TWM (F = 0.60)	B1243	1.35	1480	6	C	gl (98), ol (2)	0.15
TWM (F = 0.60)	B1245	1.35	1440	6	C	gl (90), ol (10)	0.08
TWM (F = 0.60)	B1265	1.35	1440	6	C + Pt	gl (92), ol (8), opx (0)	0.49
TWM (F = 0.60)	B1250	1.35	1400	24	C	gl (83), ol (11), opx (6)	0.08
TWM (F = 0.60)	**B1271**	**1.35**	**1360**	**31**	**C + Pt**	**gl (65), ol (11), opx (25)**	**0.39**
JD (F = 0.40)	B1247	0.85	1450	6	C	gl (100)	–
JD (F = 0.40)	B1248	0.85	1410	7	C	gl (93), ol (7)	0.06
JD (F = 0.40)	B1282	0.85	1390	24	C + Pt	gl (92), ol (8)	0.95
JD (F = 0.40)	B1251	0.85	1370	20	C	gl (70), ol (14), opx (17)	0.12
JD (F = 0.40)	B1262	0.85	1350	48	C + Pt	gl (90), ol (10), opx (0)	0.07
JD (F = 0.40)	B1264	0.85	1300	48	C + Pt	gl (55), ol (9), opx (36)	0.32
LPUM (F = 0.55)	B1293	1.20	1580	4	C + Pt	gl (100)	–
LPUM (F = 0.55)	B1289	1.20	1540	4	C + Pt	gl (95), ol (5)	0.09
LPUM (F = 0.55)	B1298	1.20	1500	8	C + Pt	gl (76), ol (12), opx (13)	0.05
LPUM (F = 0.55)	B1294	1.20	1480	19	C + Pt	gl (78), ol (15), opx (7)	0.31
LPUM (F = 0.55)	B1296	1.20	1440	21	C + Pt	gl (52), ol (14), opx (34)	0.04
LPUM (F = 0.55)	**B1288**	**1.20**	**1400**	**22**	**C + Pt**	**gl (44), ol (19), opx (37)**	**0.24**
ON66	B1283	0.80	1380	4	C + Pt	gl (100)	–
ON66	B1281	0.80	1340	7	C + Pt	gl (92), ol (1), opx (7)	0.07
ON66	B1274	0.80	1320	6	C + Pt	gl (73), ol (0), opx (27)	0.02
ON66	**B1272**	**0.80**	**1300**	**27**	**C + Pt**	**gl (73), ol (4), opx (23)**	**0.03**
ON66	B1278	0.80	1280	31	C + Pt	gl (39), ol (4), pig (48), plag (10), sp (−1)	0.06
ON66	B1280	0.80	1260	31	C + Pt	gl (18), ol (5), pig (62), plag (15), sp (1)	0.03
TWM71	B1299	0.80	1380	6	C + Pt	gl (100)	–
TWM71	B1285	0.80	1340	6	C + Pt	gl (93), ol (7)	0.09
TWM71	**B1295**	**0.80**	**1300**	**22**	**C + Pt**	**gl (87), ol (10), opx (2), sp (1)**	**0.06**
TWM71	B1297	0.80	1280	22	C + Pt	gl (44), ol (11), pig* (31), aug* (0), plag (14), sp (0)	0.01
TWM71	B1292	0.80	1260	46	C + Pt	gl (10), ol (12), pig (51), plag (28)	0.26
ON66	HA01-5	0.50	1250	26	C + Pt	gl (76), ol (5), pig (17)	0.18
ON66	HA04-5	0.50	1230	50	C + Pt	gl (76), ol (4), pig (20), sp (1)	0.17
ON66	HA02-5	0.50	1215	52	C + Pt	gl (47), ol (10), pig (35), plag (9)	0.04
ON66	HA05-5	0.50	1200	22	C + Pt	gl (33), pig* (73), aug (−17)*, plag (12)	2.50
TWM71	HA01-5	0.50	1250	26	C + Pt	gl (87), ol (13)	0.56
TWM71	HA04-5	0.50	1230	50	C + Pt	gl (84), ol (14), opx (1), sp (1)	0.11
TWM71	HA02-5	0.50	1215	52	C + Pt	gl (26), ol (18), pig (31), plag (25)	0.05
TWM71	HA05-5	0.50	1200	22	C + Pt	gl (5), ol (21), pig* (10), aug* (32), plag (32)	0.10
ON72	HA04-5	0.50	1230	50	C + Pt	gl	–
ON72	**HA05-5**	**0.50**	**1200**	**22**	**C + Pt**	**gl (76), pig* (3), cpx* (15), plag (6)**	**2.14**
ON72	HA03-5	0.50	1170	67	C + Pt	gl (46), ol (4), cpx (30), plag (20)	0.00

(*continued on next page*)

Table 3 (*continued*)

Starting composition	Run	Pressure (GPa)	Temp (°C)	Duration (hrs)	Capsule	Phases	r^2
TWM95	HA01-5	0.50	1250	26	C + Pt	gl (98), opx (2)	0.37
TWM95	HA04-5	0.50	1230	50	C + Pt	gl (96), opx (4)	0.39
TWM95	HA05-5	0.50	1200	22	C + Pt	gl (25), pig* (49), cpx* (−6), plag (32)	0.82
TWM95	HA03-5	0.50	1170	67	C + Pt	gl (18), pig (49), plag (33)	0.27
LPUM88	HA01-5	0.50	1250	26	C + Pt	gl (81), opx (11), pig (9)	0.25
LPUM88	HA04-5	0.50	1230	50	C + Pt	gl (79), ol (0), opx (12), pig (9), plag (1)	0.01
LPUM88	**HA02-5**	**0.50**	**1215**	**52**	**C + Pt**	**gl (17), pig* (44), aug* (11), plag (28)**	**0.29**
ON72/05-5	HA01-3	0.30	1180	48	C + Pt	gl (94), plag (6), sp (0)	0.06
ON72/05-5	HA04-3	0.30	1155	52	C + Pt	gl (72), pig (11), plag (17)	0.27
ON72/05-5	HA05-3	0.30	1140	100	C + Pt	gl (58), pig (19), plag (23)	0.31
ON72/05-5	**HA02-3**	**0.30**	**1130**	**66**	**C + Pt**	**gl (53), pig (24), plag (23)**	**0.69**
TWM95/05-5	HA01-3	0.30	1180	48	C + Pt	gl (99), plag (1)	0.42
TWM95/05-5	HA04-3	0.30	1155	52	C + Pt	gl (84), pig (7), plag (10)	0.36
TWM95/05-5	HA05-3	0.30	1140	100	C + Pt	gl (72), pig (13), plag (15)	0.60
TWM95/05-5	**HA02-3**	**0.30**	**1130**	**66**	**C + Pt**	**gl (68), pig (17), plag (15)**	**0.95**
LPUM/02-5	HA01-3	0.30	1180	48	C + Pt	gl (93), plag (7)	0.13
LPUM/02-5	HA04-3	0.30	1155	52	C + Pt	gl (56), pig* (17), aug* (4), plag (24)	0.29
LPUM/02-5	HA05-3	0.30	1140	100	C + Pt	gl (46), pig* (22), aug* (4), plag (28)	0.10
LPUM/02-5	**HA02-3**	**0.30**	**1130**	**66**	**C + Pt**	**gl (41), pig* (20), aug* (9), plag (29)**	**0.42**
ON/02-3 gl	HA02-1.5	0.15	1100	48	C + Pt	gl (98), plag (2)	0.31
ON/02-3 gl	HA01-1.5	0.15	1080	88	C + Pt	gl (72), pig* (38), aug* (−23), plag (12), sil (0)	0.14
ON/02-3 gl	HA03-1.5	0.15	1060	120	C + Pt	gl (50), pig (24), plag (23), sil (3)	0.04
ON/02-3 gl	**HA04-1.5**	**0.15**	**1040**	**132**	**C + Pt**	**gl (44), pig* (28), aug* (4), plag (22), sil (3)**	**0.09**
TWM/02-3	HA02-1.5	0.15	1100	48	C + Pt	gl (99), plag (1)	0.83
TWM/02-3	HA01-1.5	0.15	1080	88	C + Pt	gl (53), aug* (20), plag (18), sil (4), Fe (6)	0.04
TWM/02-3	HA03-1.5	0.15	1060	120	C + Pt	gl (58), pig* (17), aug* (6), plag (18), sil (1)	0.01
TWM/02-3	**HA04-1.5**	**0.15**	**1040**	**132**	**C + Pt**	**gl (54), pig* (11), aug* (17), plag (18), sil (1)**	**0.06**
LPUM/02-3	HA02-1.5	0.15	1100	48	C + Pt	gl (98), pig (0) plag (2)	0.13
LPUM/02-3	HA01-1.5	0.15	1080	88	C + Pt	gl, aug*, plag, sil, ilm	
LPUM/02-3	HA03-1.5	0.15	1060	120	C + Pt	gl, pig*, aug*, plag, sil, ilm	
LPUM/02-3	**HA04-1.5**	**0.15**	**1040**	**132**	**C + Pt**	**gl (49), aug (27), plag (19), sil (4), ilm (1)**	**0.10**
ON/04-1.5	HA02-0.8	0.08	1020	120	C + Pt	gl (62), ol (10), aug (11), plag (13), sil (4)	0.27
TWM/04-1.5	HA02-0.8	0.08	1020	120	C + Pt	gl, ol, aug, plag, sil, ilm	
LPUM/04-1.5	HA02-0.8	0.08	1020	120	C + Pt	gl, ol, aug, plag, sil, ilm	

Bold: experiments used as a starting composition for the following crystallization step.
pig* and aug* are used to indicate pyroxenes with a continuous range of Ca content. Pig* is the average composition of data with a wollastonite content below 20, aug* is the average pyroxene with a wollastonite content above 20.

is on the cotectic olivine + orthopyroxene for experiments in graphite capsule (contamination by up to 1 wt.% Na_2O), and in the stability field of orthopyroxene for experiments in graphite + Pt capsules. Experiments contaminated by Na have not been used to define phase equilibria. Only experiments that included an outer Pt capsule were used to define LMO phase equilibria.

$BaCO_3$ was used as the pressure medium. Pressure was calibrated against the reaction: anorthite + gehlenite + corundum = Ca-tschermak pyroxene (Hays, 1966) and found to require no pressure correction. Pressures are thought to be accurate to ±50 MPa. The temperature was measured by a Type D thermocouple, and is thought to be accurate to ±10 °C. Experiments were pressurized to 0.8 GPa at room temperature, and then the temperature was raised to 865 °C at 100 °C/min. The experiments were held at these conditions for 6 min, then the pressure was increased to the desired value and the temperature was raised to the final run conditions at 50 °C/min. The sample was held at isothermal conditions for the duration of the experiment. Experimental durations ranged from 5 to 50 h. Experimental liquids were "pressure quenched" by simultaneous power termination and decompression to ca. 1 GPa. The oxygen fugacity of our experimental setup has been constrained to be CCO-0.8 ± 0.3 in the P-T range investigated in this study (Médard et al., 2008).

Medium pressure experiments (≤0.5 GPa) have been conducted in an internally-heated pressure vessel at the University of Hannover, Germany (Berndt et al., 2002). Pure Ar was used as pressure medium. Experiments were run using a double capsule technique with the powder

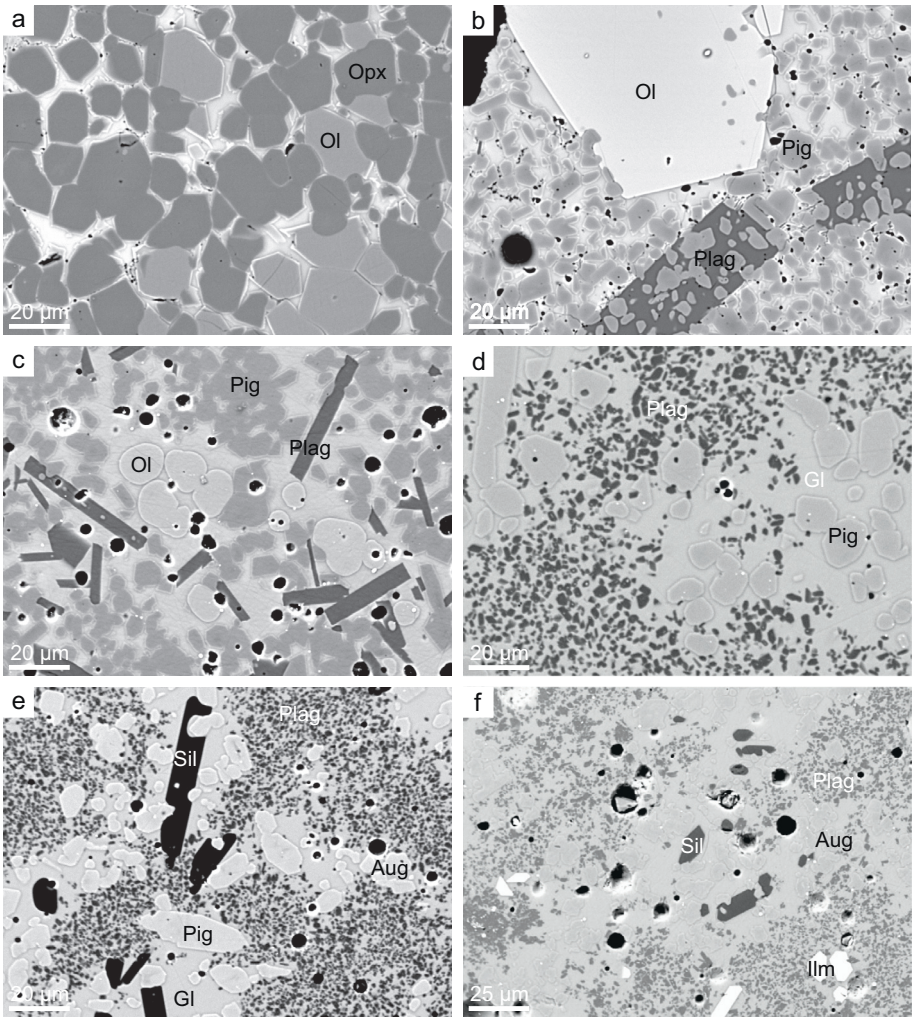

Fig. 4. Back-scattered electron images of experimental products. (a) Experiment B1266 (LPUM; 1350 °C – 1.10 GPa) with glass, olivine and orthopyroxene; (b) Experiment B1278 (ON66; 1300 °C – 0.80 GPa) with glass, olivine, pigeonite, plagioclase and spinel; (c) Experiment HA02-5 (ON66; 1215 °C – 0.50 GPa) with glass, olivine, pigeonite and plagioclase; (d) Experiment HA05-3 (ON66; 1140 °C – 0.30 GPa) with glass, pigeonite and plagioclase; (e) Experiment HA03-1.5 (ON; 1060 °C – 0.15 GPa) with glass, pigeonite, augite, plagioclase and tridymite; (f) Experiment HA01-1.5 (LPUM; 1080 °C – 0.15 GPa) with glass, augite, plagioclase, trydimite and ilmenite. Note the decrease in average crystal size between experiments performed in piston cylinder ($\geq$0.8 GPa; a–b) and experiments performed in internally-heated pressure vessel ($\leq$0.5 GPa; c–f). Gl = glass; Ol = olivine; Opx = orthopyroxene; Pig = pigeonite; Pl = plagioclase; Aug = augite; Sil = silica phase (tridymite); Ilm = ilmenite.

(ca. 15 mg) contained into a graphite capsule (2.5 mm inner diameter) enclosed into a Pt jacket (4 mm inner diameter). The large volume and the length of the hotspot (ca. 2.5 cm) enable us to run up to 5 capsules simultaneously. The samples were fixed to a Pt wire in the hot spot of the furnace. The vessel was pressurized at room temperature to the final pressure and then heated isobarically. Temperature was increased with a ramp of 30 °C/min up to 100 °C, then 50 °C/min to a temperature 30 °C below the final temperature. At this stage, temperature was kept constant for 2 min and then increased to the final temperature with a ramp of 20 °C/min. For experiments below 1100–1140 °C, we found that it was important to maintain the starting material ca. 10 °C above its liquidus temperature for ca. 1 h to ensure complete melting. Temperature was controlled using two Type S thermocouples (Pt-$Pt_{90}Rh_{10}$) connected to the Eurotherm that controls the power supply of the two furnace windings. Two additional Type S thermocouples at the bottom and top of the samples were used to monitor the actual temperature of the sample. Temperature gradient across the sample was generally less than 5 °C. Temperature distribution of the thermocouples was recorded with a time step of 1 s and in most experiments, oscillations of less than 3 °C throughout the experiment were observed. Quenching was performed by fusing the Pt-wire and dropping the capsules onto a cold copper block placed at the bottom of the sample holder. Quench rate is estimated to be ca. 150 °C/s.

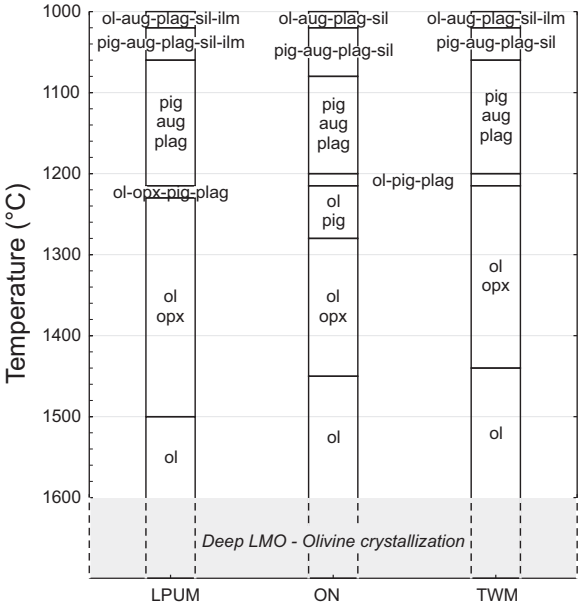

Fig. 5. Crystallization sequence expressed as a function of temperature for the lunar magma ocean obtained experimentally for three bulk Moon compositions: the Lunar Primitive Upper Mantle (LPUM), the O'Neill composition (ON), and the Taylor Whole Moon (TWM). Abbreviations are as in Fig. 4.

5.3. Analytical methods

Compositions of the minerals and glasses from piston-cylinder experiments were analyzed using wavelength dispersive spectrometry on the 5-spectrometer JEOL 8200 electron microprobe at MIT. Natural and synthetic primary and secondary standards were used, and the CITZAF online data correction package was used for all analyses (Armstrong, 1995). Analyses were performed with a 15 kV accelerating voltage and a beam current of 10nA, utilizing a beam spot size of ca. 2 μm. For glasses we used a 10 μm defocused beam, 10nA beam current and 15 kV accelerating voltage.

Analyses of experimental charges from IHPV experiments were performed with a Cameca SX-100 electron microprobe at the University of Hannover. Glasses were measured with a 15 kV and 8nA beam with a spot size of 10 μm in most experiments. Peak counting times were 20 s for major elements and 40 s for minor elements. Minerals were measured with a focused (1μm) 15 kV and 15nA beam. Peak counting times were 20 s for each element. The following standards were used for Kα X-ray line calibration of glasses and minerals: wollastonite for Si and Ca, TiO_2 for Ti, Al_2O_3 for Al, Fe_2O_3 for Fe, Mn_3O_4 for Mn, MgO for Mg, albite for Na, orthoclase for K, Cr_2O_3 for Cr. Raw data were corrected with the CATZAF software. The complete dataset for mineral and glass analyses is reported in Supplementary Table S1.

6. RESULTS

6.1. Phase equilibria

Experiments have been performed on a range of LMO compositions and from these experiments systematic observations can be made about phase equilibria (Table 3; Fig. 4). For most investigated primitive compositions (obtained by subtraction of olivine), olivine is the first liquidus phase followed by orthopyroxene. A few compositions (e.g. ON 0.44) lie in the stability field of orthopyroxene, meaning that too much olivine had been subtracted from the LMO parental liquid and that residual liquid that we calculated has overstepped the olivine + orthopyroxene boundary. These experiments cannot be used to constrain the sequence of crystallization of the LMO but are useful for the calculation of the orthopyroxene/liquid partitioning. With decreasing temperature and pressure, olivine stays on the liquidus with orthopyroxene in a cotectic assemblage. Orthopyroxene is then replaced by pigeonite. The appearance of pigeonite is simultaneous with that of plagioclase (1280–1240 °C). Very minor Cr-rich spinel is observed in a few experiments. For most compositions, olivine disappears below 1200 °C and sub-calcic augite appears. It should be noted that pyroxene compositions display a range of CaO content in a single experimental charge, making it difficult to discriminate clearly between pigeonite and sub-calcic augite (Supplementary materials). This has been previously reported in experiments on lunar magmas and in natural samples from the Moon (e.g. Grove and Bence, 1979; Joy et al., 2006). The compositional range observed in pyroxenes is explained by the extremely small differences in free energy between Ca-rich pigeonite and Ca-poor augite near the apex of the miscibility gap so that relatively rapid crystallization allows metastable intermediates to grow (Lindsley and Munoz, 1969; Sack and Ghiorso, 1994). The assemblage containing glass, pigeonite, sub-calcic augite and plagioclase is followed by the crystallization of a silica phase (at 1080 °C), and then by ilmenite. In our lowest temperature experiments (1020 °C), olivine is stable again and pigeonite disappears. Both the earlier low-Ca pyroxene + olivine solidification stages and the later stages of crystallization with plagioclase, pyroxenes, silica phase and ilmenite, do not change significantly for the LPUM, ON and TWM bulk Moon compositions.

The sequences of crystallization produced in our experiments are illustrated in Fig. 5 that summarizes our experimental observations and the succession of cumulus assemblages during cooling of LPUM, ON, and TWM compositions. However, they do not mirror strictly the relative volumes of cumulate packages that form as the LMO crystallized. Indeed, the studied bulk Moon compositions have different profiles for liquidus temperature vs. fraction of residual liquid. For example, although plagioclase appears at higher temperature in the LPUM composition, the total mass of plagioclase that will crystallize from the TWM composition would be greater.

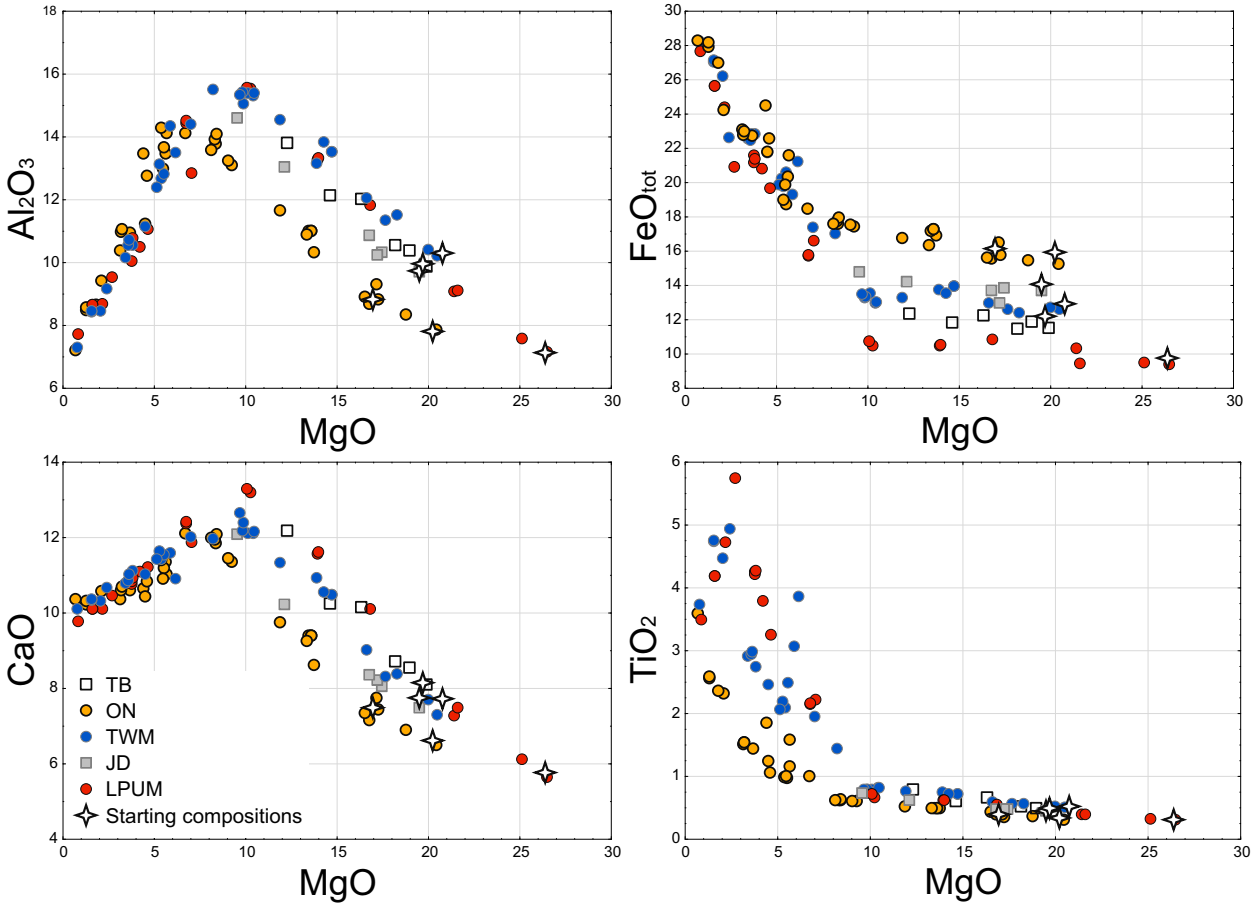

Fig. 6. Compositions of experimental liquids illustrating the polybaric liquid lines of descent for different bulk Moon compositions (see Table 1 for references). Starting compositions (stars) are residual melts calculated by subtraction of olivine to bulk Moon (Table 2).

6.2. Composition of experimental liquids

Electron microprobe analyses for all experimental liquids are reported in Supplementary Table S1. Compositional trends for selected major elements are displayed in Fig. 6. Liquids show continuous MgO depletion with temperature from 32–38 wt.% in bulk Moon (Fig. 2), to 17–26 wt.% in parental liquids calculated by subtracting olivine from the bulk Moon compositions, and then to less than 1 wt.% in the most evolved residual melts at 1020 °C. Silica remains approximately constant during crystallization (roughly between 46 and 50 wt.%). The polybaric liquid lines of descent (see experimental strategy above) can basically be subdivided into two stages: before and after plagioclase saturation. Before plagioclase crystallization, the trends display Al_2O_3 and CaO enrichment, with moderate increase in FeO_{tot}. After plagioclase saturation, the paths followed by the residual liquids show Al_2O_3 and CaO depletion and residual liquids record extreme iron enrichment up to 28 wt.% FeO_{tot}. Most noticeable is that residual melts do not show FeO_{tot} depletion after ilmenite saturation. The amount of TiO_2 in the melt increases continuously until ilmenite saturation (at 1080 °C in LPUM and 1020 °C in TWM) and then drops. After plagioclase saturation, the residual liquids from the different starting bulk Moon compositions converge on common liquid line of descents with production of ferrobasalts. This suggests the existence of a thermal valley, as already observed by Hess et al. (1975) based on fractional crystallization experiments on high-titanium, low-titanium, and KREEP basalts.

6.3. Parametrization of the forward modelling

Modeling the evolution of melts in the LMO requires that we define criteria to identify the appearance or disappearance of liquidus phases. These criteria can be based on theoretical calculations of phase stability in the liquid (Snyder et al., 1992; Elkins-Tanton et al., 2011), or on appropriate fractional crystallization experiments as presented in this study. Here, we use temperature as the criteria to define conditions for the successive appearance of cumulus assemblages for each bulk Moon composition (see Supplementary Materials). A thermometer based solely on the composition of the melt and the pressure is proposed using our experimental dataset (see Supplementary Materials). With our new thermometer, we are able to predict the temperature of the LMO residual melts with a standard error of estimate of 19 °C. For ilmenite, we could not define a single temperature of liquidus saturation. We however observed that the temperature of ilmenite saturation in our experi-

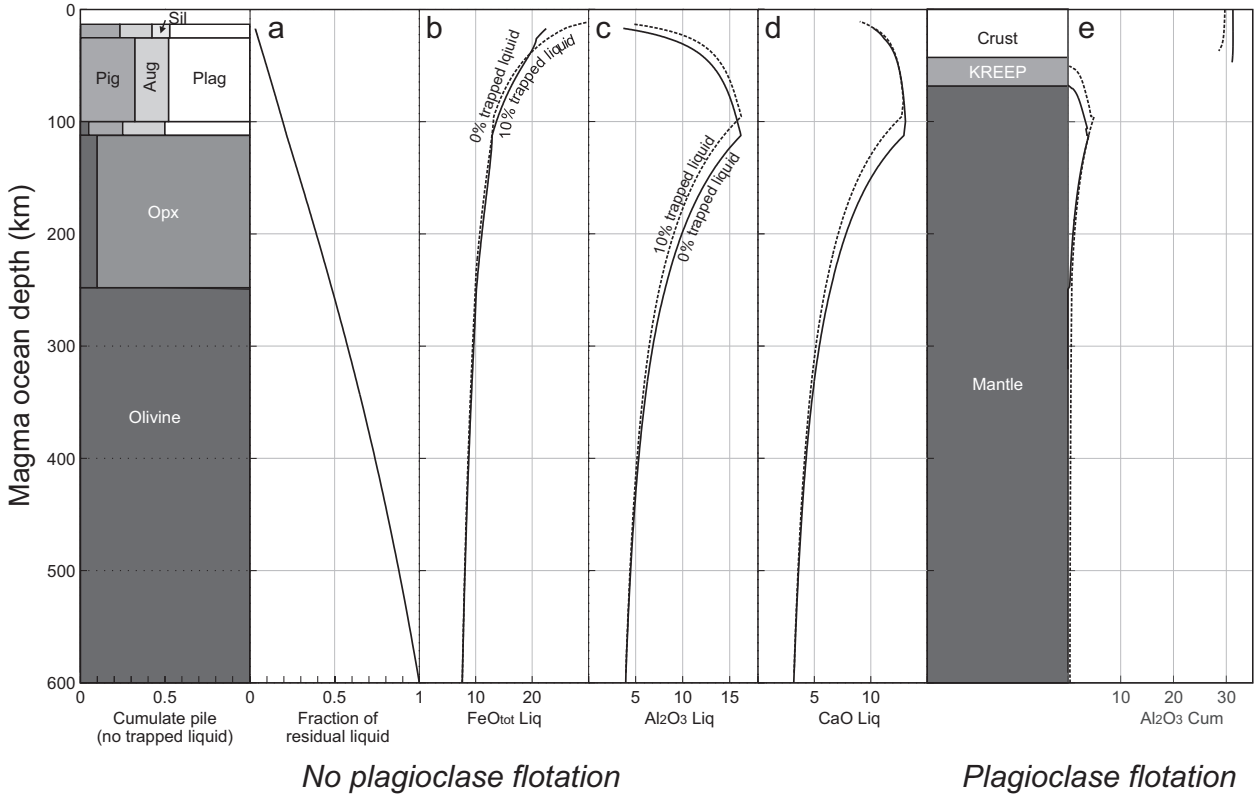

Fig. 7. Stratigraphy of the lunar magma ocean as obtained by the forward modelling on the alkali-depleted Earth-like bulk Moon composition (LPUM composition of Longhi, 2006). (a) Fraction of residual liquid; (b) FeO_{tot}, (c) Al_2O_3 and (d) CaO (wt.%) in residual liquids calculated with 0% and 10% trapped liquid in cumulates; (e) Al_2O_3 (wt.%) in the cumulate assuming 0% and 10% trapped liquid and complete flotation of plagioclase and the silica phase. No flotation of plagioclase and silica is assumed in panels a–d.

ments could be accurately estimated using a multiple linear regression that takes into account the TiO_2, FeO and MgO contents of the melts.

The experimental dataset presented in this study is also used to constrain crystal/liquid partitioning for melt compositions under P-T conditions relevant for the evolution of the LMO. The most important variables for which we needed new experimental constraints in order to construct a model are the distribution coefficients for Fe and Mg between ferromagnesian silicates and melt, and the aluminum, calcium and titanium content in pyroxenes in the conditions of LMO solidification. Our experimental dataset contains 42 olivine-melt pairs, 31 orthopyroxene-melt pairs, 32 pigeonite-melt pairs, 21 sub-calcic augite-melt pairs, and 5 ilmenite-melt pairs. Based on these experiments, we regressed new predictive equations for the distribution of major elements between crystal and liquid for olivine, orthopyroxene, pigeonite, plagioclase, augite, ilmenite, and tridymite. The equations are detailed in the Supplementary Materials.

The instantaneous proportions of crystallizing liquidus phases are also key parameters in the forward model for the evolution of liquids in the LMO. This parameter also defines the density profile of the lunar mantle. Mass balance calculations using two liquids with the same cumulus assemblages but different degrees of crystallinity (one at higher and one at lower temperature) can be used to calculate cotectic proportions. These proportions can also be estimated by trial and error until the evolution of experimental melts (Fig. 6; the polybaric liquid line of descent) is reproduced by the forward modelling approach. Cotectic proportions considered in this study have been obtained by combining the two methods (see Supplementary Materials).

The volume and densities of minerals have been calculated at the pressure of interest at the solidus of the crystallizing LMO. This is an accurate representation of the actual volume of cumulate rocks because minerals will shrink (according to their coefficients of thermal expansion) during progressive cooling from their initial temperature of crystallization along the liquidus of the melt to subsolidus temperature. This effect however becomes less important as temperature decreases (Erba et al., 2015). The LMO cumulate solidus has been estimated using the MELTS/pMELTS thermodynamic algorithms (Ghiorso and Sack, 1995; Ghiorso et al., 2002) on the LPUM bulk Moon composition (Table 1) and its residual experimental melts at the appropriate pressure (Table 2). As crystallization proceeds bottom up, the solidus (we considered a residual liquid proportion of 0.5%) for the liquid evolving by fractional crystallization follow the equation: $T_{solidus}$ (°C) = 823.29 + 1896.92 * F – 436.21 * P (r^2 = 0.996; SEE = 20.5 °C), with F the fraction of residual liquid (wt.%) of the LMO and P the pressure (GPa).

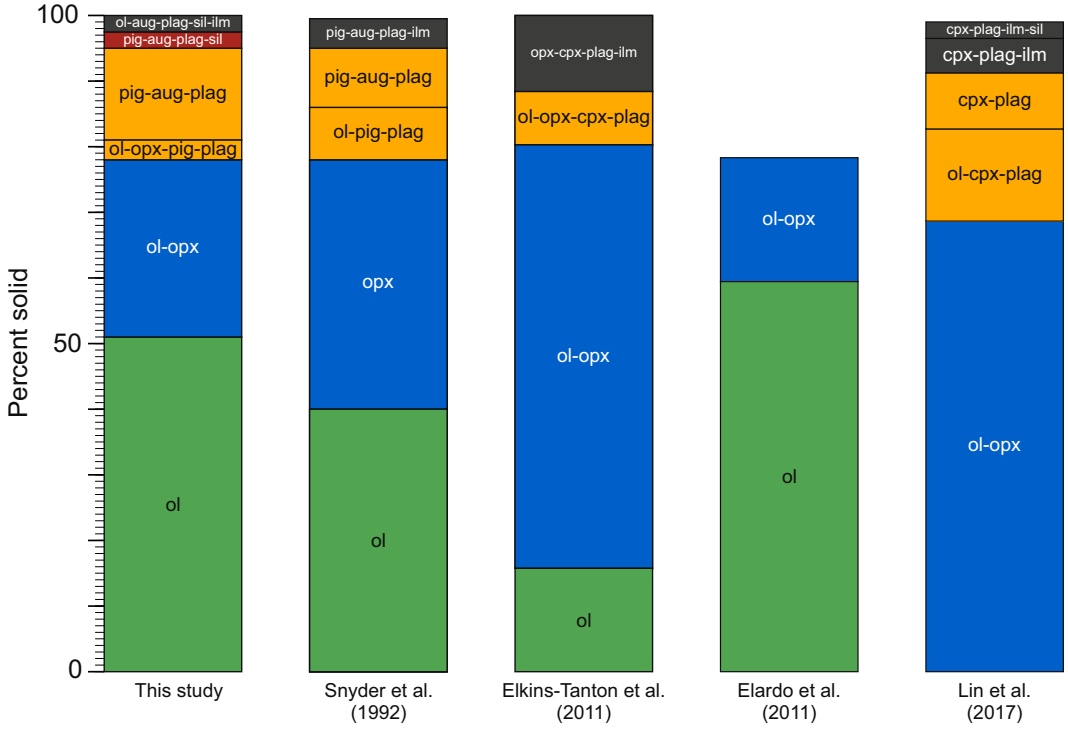

Fig. 8. Comparative cumulate stratigraphy for solidified lunar magma oceans. Early layers only contain olivine (green) and/or orthopyroxene (blue). Middle layers are defined by the appearance of plagioclase (orange), and late layers are defined by the appearance of a silica-phase (red) and ilmenite (grey). Abbreviations are as in Fig. 4. (For interpretation of the references to colour in this figure legend, the reader is referred to the web version of this article.)

7. DISCUSSION

7.1. Stratigraphy and liquid line of descent of the LMO

Forward modelling of the liquid line of descent and the crystallization products for a 600 km-thick alkali-depleted Earth-like (LPUM) LMO is illustrated in Fig. 7. Modelling was performed by assuming 0–10% of trapped liquid in the cumulate mantle rocks. Crystallization starts with a very large volume of olivine cumulate because we made the assumption that fractional crystallization starts from the early stages of LMO solidification. It is followed by orthopyroxene-olivine cumulates, both phases having a cotectic relationship. This early crystallizing sequence is nearly identical to that assumed by Elkins-Tanton et al. (2011), although orthopyroxene appears earlier (deeper) in that model because of the pressure effect on the relative stability of olivine and orthopyroxene in a 1000 km thick LMO (as opposed to 600 km in our study). Plagioclase appears at a residual liquid fraction of $F = 0.22$ for pure fractional crystallization and at $F = 0.19$ if 10% trapped liquid is assumed. We stop the model at 1020 °C corresponding to $F = 0.02$. The last 11 km of the LMO are considered to represent the KREEP-like component. As already displayed in Fig. 6, the saturation of plagioclase (and subcalcic augite) in the upper 100 km causes a major depletion in Al_2O_3 and CaO in residual liquids.

We also illustrate the crystallization column if plagioclase flotation is considered. As previously shown by other studies (e.g. Warren, 1990), the density of plagioclase is lower compared to the equilibrium liquid in the lunar magma ocean (density of 2.80–2.88 g/cm^3 after plagioclase saturation). Complete flotation (100% efficiency) is assumed in Fig. 7 and clear distinction between the mantle, the KREEP component and the crust can be made. Alumina is dramatically concentrated in the plagioclase crust, although a significant amount (up to 5 wt.%) is concentrated in the part of the LMO cumulate upper mantle that is dominated by pyroxenes. This is in agreement with the observation that the upper mantle exposed in the South Pole-Aitken basin is dominated by low-calcium pyroxene (Melosh et al., 2017). The thickness of the floating anorthosite crust depends strongly on several parameters that are discussed thoroughly in the next sections.

In Fig. 8, we compare the cumulate stratigraphy for the solidified lunar magma ocean proposed in this study to those reported in the literature (Snyder et al., 1992; Elkins-Tanton et al., 2011; Elardo et al., 2011; Lin et al., 2017). Differences between these columns are the results of different approaches (experiments vs. modelling) and parameters (e.g. whole Moon compositions, magma ocean depth…). However, broad comparisons can be made. We first note that the basal cumulate sequence is dominated by olivine and orthopyroxene ± olivine. The early sequence of Lin et al. (2017) is formed of olivine + orthopyroxene because it assumes equilibrium crystallization during the first stages of LMO crystallization. Plagioclase appears

after 78–81% solidification in our study and in those of Snyder et al. (1992) and Elkins-Tanton et al. (2011). Plagioclase crystallization starts significantly earlier in the model of Lin et al. (2017) (after 68% solidification). Attention should also be dedicated to the succession of pyroxenes as three types can be clearly distinguished: orthopyroxene (hypersthene), pigeonite and sub-calcic augite. A noticeable difference in cumulate stratigraphy is the formation of a silica phase in the late-stage cumulates of our study and of Lin et al. (2017; see discussion below). We note that the silica phase has been identified in the two experimental studies on liquid compositions appropriate for the LMO evolution. Finally, ilmenite saturation is reached after 97% solidification in our study, which is slightly later compared to previous work.

7.2. Alumina in the mantle and residual melts

The alumina stored in the mantle needs to be quantified in order to estimate the amount available for the crystallization of plagioclase, with direct implications for crustal thickness. Aluminum in olivine is negligible so that orthopyroxene accounts for the Al budget before plagioclase appearance. Our experimental dataset has orthopyroxene stable between 1.35 and 0.50 GPa, and from 1500 to 1230 °C. Experiments show that orthopyroxene has a cotectic relation with olivine, which differs from the peritectic relation in the model of Snyder et al. (1992) that considered crystallization at 6 kbar. Alumina may also be retained in the lunar mantle in residual liquid trapped during early cumulate formation. Melts in equilibrium with olivine-orthopyroxene cumulate contain 9–15 wt.% Al_2O_3 (Supplementary Table S1), so that, considering a potential range of trapped liquid content up to 10% (Snyder et al., 1992; Elkins-Tanton et al., 2011), the aluminum retained additionally in the mantle because of trapped melt can reach 1.5 wt.%. Modeling the mantle composition for alumina including the amount stored in orthopyroxene and in the trapped liquid is presented in Fig. 7c,e. Aluminum in the residual melt at plagioclase saturation is about 16 wt.%. A deeper magma ocean would be responsible for an earlier appearance of orthopyroxene because pressure enhances the stability of orthopyroxene over that of olivine (Warren and Wasson, 1979a; Longhi, 1981). This would have the consequence of storing more alumina in orthopyroxene in the deeper mantle. However, the Al content of orthopyroxene is low and this would therefore not counteract the effect of a deeper magma ocean which is the crystallization of larger volume of plagioclase that will ultimately produce a thicker crust.

We note that the amount of trapped liquid in the cumulate pile has an important effect on the Al budget which has some implications for the crustal thickness. In this study we investigate the effect of a reasonable range of trapped liquid from 0 to 10% as commonly discussed (e.g. Elkins-Tanton et al., 2011). Ultramafic rocks (olivine-bearing) are expected to form adcumulates with porosities in the order of 5% (e.g. Schmidt et al., 2012). The trace element signature of mare basalts also indicates the presence of trapped melt in their source regions with values <3% (Snyder et al. 1992) or even <1% (Elardo et al., 2014). Independent calculations on volatiles in lunar rocks suggest that any amount of trapped liquid higher than about 1% would increase the Cl/H_2O and Cl/F ratios in the mantle to values much higher than are permitted by the observed ratios in mare basalts (McCubbin et al., 2015). Consequently, our models assuming 10% trapped liquid should be viewed as an extreme end-member while a value <3% is a more reasonable scenario.

7.3. Crystallization of a silica phase in the LMO

A major feature common to the late-stage differentiation of all bulk Moon compositions is the presence of a silica phase (most probably tridymite) at 1080 °C and below. It appears before ilmenite for all compositions. The maximum Mg-number of pigeonite is 40 and the lowest temperature experiments (1020 °C) contain olivine $Fo_{9\text{-}11}$. The presence of a silica phase has often been described in experiments relevant for the late-stage evolution of the Moon (Hess et al., 1975; Longhi, 2003), and in lunar ferrobasalts (Grove and Bence, 1979). A silica phase was also identified in the LMO experiments of Lin et al. (2016).

This observation has major implications. Indeed, when considering the canonical magma ocean model with plagioclase flotation that form the anorthosite crust, a low-density silica phase in the liquidus assemblage should be part of the floating cumulate. The relative proportions of plagioclase and tridymite are in the range 90/10–95/5, based on mass-balance calculations in our experiments. However, tridymite appears on the liquidus ca. 200–150 °C after plagioclase so that significant amounts of pure anorthosite (without tridymite) should be produced before the potential formation of tridymite-bearing anorthosite. Stratigraphically, tridymite-bearing anorthosite would thus occur deeper in the plagioclase-rich crust below the pure anorthosite, commonly observed at the surface of the Moon (Ohtake et al., 2009). Tridymite-bearing anorthosite might thus be observable in deep craters where the base of the anorthosite crust has been exposed.

Silica phases are rare in feldspathic lunar anorthosites (Korotev et al., 2003), but silicic volcanic landforms have been identified at the lunar surface by remote sensing methods (Glotch et al., 2010, 2011; Jolliff et al., 2011). The presence of a silica phase in primordial lunar magma ocean cumulates also constitutes a source for the production of granitic lithologies (Rutherford et al., 1976; Warren et al., 1983; Jolliff et al., 1999; Seddio et al., 2013).

7.4. Crustal thickness

The uncertainties on the depth of the magma ocean result from the uncertainties in our knowledge of the bulk Al_2O_3 content of the LMO, the thickness of the anorthositic crust and its average plagioclase fraction. In their review of lunar seismological data Wieczorek et al. (2006) advocated for an average crustal thickness of 49 ± 16 km. Consideration of the new data provided by GRAIL on the thickness

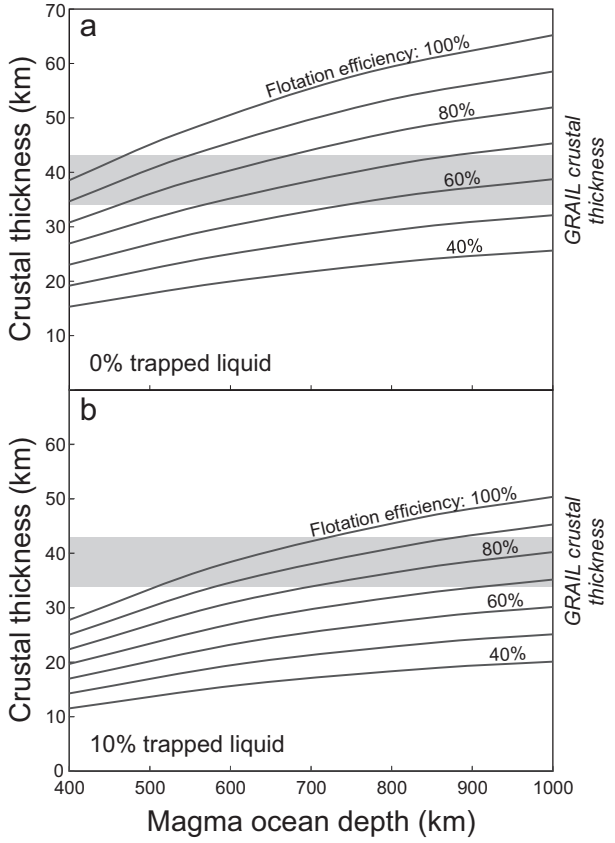

Fig. 9. Calculation of the thickness of the anorthosite crust as a function of lunar magma ocean depth and flotation efficiency of plagioclase (80% meaning that 80 wt.% plagioclase floated to form the anorthositic crust and 20 wt.% accumulated on the floor of the LMO). Calculation were performed with (a) 0% trapped liquid and (b) 10% trapped liquid in both basal and floated cumulates. The silica phase that crystallized from the late state liquids of the LMO is included in the floated cumulate (although its contribution to the crust is minor). The GRAIL crustal thickness (34–43 km) is from Wieczorek et al. (2013).

of the crust indicates that the crust is thinner than previously thought (40 km). With such a thin plagioclase-rich crust it is hardly conceivable that the whole Moon has melted because it would have produced significantly thicker crust (up to 70 km, Shearer et al., 2006). This would be true if the bulk composition was a refractory-enriched or an Earth-like lunar composition (Longhi, 2006).

Our forward model approach enables us to propose a range of possible scenarios that can produce an anorthositic crust that matches the 40 km thick GRAIL estimate (Wieczorek et al., 2013). Several variables may affect the amount of plagioclase accumulated at the top of the LMO: the depth of the LMO, the amount of liquid trapped in cumulates, which controls the volume of residual magma at the appearance of liquidus plagioclase, and the efficiency of plagioclase flotation. A shallower magma ocean will provide less Al_2O_3 to form the plagioclase crust. Al_2O_3 is also partitioned into mantle minerals (particularly pyroxenes) and may be trapped in the interstitial liquid so that the bulk alumina does not fully contribute to plagioclase crystallization and crust formation. Additionally trapping of buoyant plagioclase at the floor of the LMO has been suggested to some extent (2–5%; Snyder et al., 1992) to account for the observed Al and trace-element concentrations in mare basalts. Appropriate conditions for efficient plagioclase flotation have been discussed by Suckale et al. (2012). Specific parameters for crystal size, crystal fraction in suspension, and density difference between crystals and liquid are necessary to allow efficient plagioclase flotation. Low viscosity magmas during the late-stage evolution of the lunar magma ocean also contribute to increase the efficiency of plagioclase segregation (Dygert et al., 2017). It has also been discussed that flotation of buoyant plagioclase in magma chambers on Earth might be an inefficient process due to in situ crystallization at the floor rather than along the adiabat (Namur et al., 2011). In situ crystallization along the floor of the LMO may prevent plagioclase flotation by the formation of coherent three dimensional chains of crystals (Philpotts et al., 1998). In the Sept Iles layered intrusion, the flotation efficiency of buoyant plagioclase has been shown to be smaller than 50%, and a similar efficiency was previously proposed for the Moon (Namur et al., 2011).

Fig. 9 illustrates our calculations of the thickness of the anorthosite crust (plagioclase + silica phase) formed by flotation after solidification to 1020 °C of the lunar magma ocean (corresponding to 98% crystallization) as a function of magma ocean depth and flotation efficiency. Cotectic proportions for plagioclase are between 50 and 42 wt.% depending on the phase assemblage (see Supplementary Materials) and 10% for the silica phase. Trapped liquid fractions of 0 and 10% are considered in the calculations. Fig. 9 shows that a relatively shallow magma ocean (<700 km) is necessary to explain the thin crust revealed by GRAIL if perfect plagioclase flotation is assumed. A depth of 500 km is necessary even if no trapped liquid is considered. However, for imperfect efficiency of plagioclase flotation deeper magma oceans can produce thinner crusts. As an example, a 1000 km thick magma ocean can produce a 40 km thick anorthositic crust if the flotation efficiency is 80% and if 10% trapped liquid is assumed. In these calculations, the silica phase is considered to contribute to building the crust but it remains a minor component of the lower crust.

It has been recently suggested by Lin et al. (2016) that an early wet Moon was responsible for the formation of the thin lunar crust as measured by GRAIL (Wieczorek et al., 2013). We concur that it has been known that water in basaltic magmas effectively delays the saturation of plagioclase compared to mafic phases (e.g. Sisson and Grove, 1993; Almeev et al., 2012). However, the volume of plagioclase formed during crystallization of the LMO mainly depends on the normative plagioclase component of the bulk Moon composition and not on magmatic water contents. Indeed, providing that the main alumina-bearing mineral that crystallizes is plagioclase, the delay in plagioclase saturation will produce Al_2O_3-enrichment in residual liquids but these residual liquids will then crystallize more plagioclase before the solidus is reached. Although the global occurrence of spinel has been detected at the surface of

the Moon (Pieters et al., 2011; Sun et al., 2017), its formation is not related to primary crystallization products of the LMO but is explained by impact melting or by the interaction of Mg-suite parental melts with the anorthositic crust (Gross and Treiman, 2011; Prissel et al., 2014). Consequently, a thin lunar crust does not support a wet Moon hypothesis. Other, more direct evidence has been presented to argue for very small H-contents in lunar magmas (Saal et al., 2008; Hui et al., 2013b; McCubbin et al., 2015).

7.5. The nearside-farside dichotomy and magnesian anorthosites

The surface of the Moon displays an obvious dichotomy with abundant volcanic maria on the nearside and heavily-cratered highlands on the farside. These regions also have different properties such as crustal thickness with the farside being significantly thicker (Zuber et al., 1994; Ishihara et al., 2009) and compositionally distinct (Jolliff et al., 2000; Ohtake et al., 2012). The anorthositic lunar highlands display different compositional ranges with the farside displaying significantly higher Mg-number values (Ohtake et al., 2012). The origin of this dichotomy has been suggested to be linked with magma ocean processes due to spatial variations in tidal heating when the crust was decoupled from the mantle by a liquid horizon (Garrick-Bethell et al., 2010) and/or asymmetric crustal growth with the first more primitive crustal section being formed preferentially on the farside of the Moon (Ohtake et al., 2012).

Our forward model of magma ocean solidification enables us to constrain the degree of evolution that is necessary to produce compositional characteristics of the nearside and farside of the Moon. We have shown that, for an alkali-depleted Earth-like composition, plagioclase appears for a fraction of residual liquid of F = 0.22 (or F = 0.19 if 10% trapped liquid is assumed). Plagioclase saturation in the LMO marks the onset of crust building because of plagioclase flotation in a dense FeO-enriched magma ocean. At this stage of evolution, the Mg-number of low-Ca pyroxene (pigeonite) is ca. 80–84 (Fig. 10), which corresponds to the composition of pyroxenes in the most primitive primordial anorthosite crust. This compositional range for pyroxene includes the most primitive values reported for the farside of the Moon (Ohtake et al., 2012). Fig. 10 illustrates that the range of Mg-number on the farside of the Moon (Mg-number = 45–77) can be produced when the fraction of residual liquid in the magma ocean is between 0.18 and 0.07. The more evolved Mg-number (40–71) on the nearside of the Moon needs more evolved liquids, encountered when F varies between 0.14 and 0.06. We thus concur with Ohtake et al. (2012) that asymmetric crustal growth would explain the lunar dichotomy that would be produced because of initial crustal building on the farside. We quantify that crustal formation on the nearside of the Moon by plagioclase (and silica phase) flotation was delayed compared to the farside during crystallization of 4% of the fraction of the residual LMO.

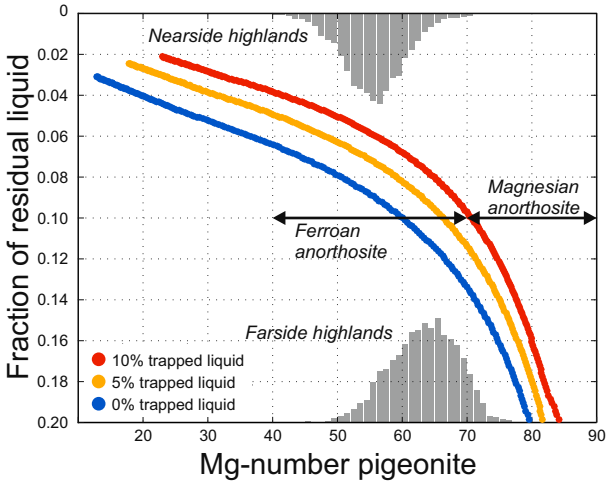

Fig. 10. Mg-number of pigeonite (low-Ca pyroxene) calculated by the forward model using the LPUM compositions for fraction of residual liquids <0.20. The model assumes 0, 5 and 10 trapped liquid in the fractionated cumulate. Histograms for the nearside and farside highlands are from Ohtake et al. (2012).

Additionally, our constraints on the Mg-number of pyroxenes after plagioclase saturation in the LMO show that magnesian anorthosites (Mg-number > 70; Takeda et al., 2006; Gross et al., 2014) can be produced from the LMO when the first liquidus plagioclase forms. Alternative processes such as serial magmatism are not required to produce these lithologies.

8. CONCLUSIONS

Our systematic experimental study on compositions relevant for the crystallization of the lunar magma ocean enables us to parametrize the crystallization sequence and the major element partitioning between residual melts and liquidus phases. These results are implemented in a forward model used to constrain controlling factors on crustal thickness. We identify a range of conditions favorable to produce the thin anorthosite crust identified by GRAIL and rule out the possibility of a whole Moon magma ocean. The LPUM bulk composition and a 600 km deep magma ocean provides the best solution of the observable variables on the Moon. Our experiments on evolved residual liquids contain a silica phase which might be an important component of the lower lunar crust. Very late stages liquids are strongly enriched in iron and ilmenite appears very late in the crystallization sequence, so that the ilmenite-bearing cumulate should be <10 km thick. The primordial crust-mantle differentiation scenario depicted in this study is based on relevant crystallization experiments and should stand as a basis when considering further evolution of the Moon, such as mantle overturn and partial melting of the interior.

ACKNOWLEDGEMENTS

BC acknowledges support by a Marie Curie International Outgoing Fellowship within the 7th European Community Framework Programme and by the Humboldt Foundation. BC is a Research

Associate of the Belgian Fund for Scientific Research-FNRS. ON acknowledges support from a Marie Curie Intra European Fellowship and from the DFG through the Emmy Noether program. TLG acknowledges support from grant 80NSSC17K0773 from the NASA Solar System Workings Program. This paper has benefited from careful reviews by Steve Elardo, John Pernet-Fischer and an anonymous referee.

APPENDIX A. SUPPLEMENTARY MATERIAL

Supplementary data associated with this article can be found, in the online version, at https://doi.org/10.1016/j.gca.2018.05.006.

REFERENCES

Almeev R. R., Holtz F., Koepke J. and Parat F. (2012) Experimental calibration of the effect of H_2O on plagioclase crystallization in basaltic melt at 200 MPa. *Am. Mineral.* **97**, 1234–1240.

Barr J. A. and Grove T. L. (2013) Experimental petrology of the Apollo 15 group A green glasses: melting primordial lunar mantle and magma ocean cumulate assimilation. *Geochim. Cosmochim. Acta* **106**, 216–230.

Beard B. L., Taylor L. A., Scherer E. E., Johnson C. M. and Snyder G. A. (1998) The source region and melting mineralogy of high-titanium and low-titanium lunar basalts deduced from Lu-Hf isotope data. *Geochim. Cosmochim. Acta* **62**, 525–544.

Berndt J., Liebske C., Holtz F., Freise M., Nowak M., Ziegenbein D., Hurkuck W. and Koepke J. (2002) A combined rapid-quench and H_2-membrane setup for internally heated pressure vessels: description and application for water solubility in basaltic melts. *Am. Mineral.* **87**, 1717–1726.

Borg L. E., Connelly J. N., Boyet M. and Carlson R. W. (2011) Chronological evidence that the Moon is either young or did not have a global magma ocean. *Nature* **477**, 70–72.

Bottinga Y. and Weill D. F. (1970) Densities of liquid silicate systems calculated from partial molar volumes of oxide components. *Am. J. Sci.* **269**, 169–182.

Boyd F. R. and England J. L. (1960) Apparatus for phase-equilibrium measurements at pressures up to 50 kilobars and temperatures up to 1750 °C. *J. Geophys. Res.* **65**, 741–748.

Brown S. M. and Grove T. L. (2015) Origin of the Apollo 14, 15, and 17 yellow ultramafic glasses by mixing of deep cumulate remelts. *Geochim. Cosmochim. Acta* **171**, 201–215.

Cameron A. G. W. and Benz W. (1991) The origin of the Moon and the single impact hypothesis IV. *Icarus* **92**, 204–216.

Canup R. M. (2012) Forming a Moon with an earth-like composition via a giant impact. *Science* **338**, 1052–1055.

Canup R. M. and Asphaug E. (2001) Origin of the Moon in a giant impact near the end of the Earth's formation. *Nature* **412**, 708–712.

Canup R. M., Visscher C., Salmon J. and Fegley, Jr, B. (2015) Lunar volatile depletion due to incomplete accretion within an impact-generated disk. *Nat. Geosci.* **8**, 918–921.

Ćuk M. and Stewart S. T. (2012) Making the Moon from a fast-spinning earth: a giant impact followed by resonant despinning. *Science* **338**, 1047–1052.

Dauphas N., Burkhardt C., Warren P. H. and Teng F.-Z. (2014) Geochemical arguments for an Earth-like Moon-forming impactor. *Philos. Trans. R. Soc. Lond. Ser. A Math. Phys. Eng. Sci.* **372**, 20130244.

Draper D. S., duFrane S. A., Shearer, Jr, C. K., Dwarzski R. E. and Agee C. B. (2006) High-pressure phase equilibria and element partitioning experiments on Apollo 15 green C picritic glass: implications for the role of garnet in the deep lunar interior. *Geochim. Cosmochim. Acta* **70**, 2400–2416.

Dygert N., Lin J. F., Marshall E. W., Kono Y. and Gardner J. E. (2017) A low viscosity lunar magma ocean forms a stratified anorthitic flotation crust with mafic poor and rich units. *Geophys. Res. Lett.* **44**, 11, 282–211, 291.

Elardo S. M., Draper D. S. and Shearer, Jr, C. K. (2011) Lunar magma ocean crystallization revisited: bulk composition, early cumulate mineralogy, and the source regions of the highlands Mg-suite. *Geochim. Cosmochim. Acta* **75**, 3024–3045.

Elardo S. M., Shearer C. K., Fagan A. L., Borg L. E., Gaffney A. M., Burger P. V., Neal C. R., Fernandes V. A. and McCubbin F. M. (2014) The origin of young mare basalts inferred from lunar meteorites Northwest Africa 4734, 032, and LaPaz Icefield 02205. *Meteorit. Planet. Sci.* **49**, 261–291.

Elkins-Tanton L. T. (2012) Magma oceans in the inner solar system. *Ann. Rev. Earth Planet. Sci.* **40**, 113–139.

Elkins-Tanton L. T., Burgess S. and Yin Q.-Z. (2011) The lunar magma ocean: reconciling the solidification process with lunar petrology and geochronology. *Earth Planet. Sci. Lett.* **304**, 326–336.

Elkins-Tanton L. T. and Grove T. L. (2011) Water (hydrogen) in the lunar mantle: results from petrology and magma ocean modeling. *Earth Planet. Sci. Lett.* **307**, 173–179.

Elkins-Tanton L. T., Parmentier E. M. and Hess P. C. (2003) Magma ocean fractional crystallization and cumulate overturn in terrestrial planets: implications for Mars. *Meteorit. Planet. Sci.* **38**, 1753–1771.

Elkins Tanton L. T., Van Orman J. A., Hager B. H. and Grove T. L. (2002) Re-examination of the lunar magma ocean cumulate overturn hypothesis: melting or mixing is required. *Earth Planet. Sci. Lett.* **196**, 239–249.

Erba A., Maul J., Pierre M. D. L. and Dovesi R. (2015) Structural and elastic anisotropy of crystals at high pressures and temperatures from quantum mechanical methods: the case of Mg_2SiO_4 forsterite. *J. Chem. Phys.* **142**, 204502.

Gaffney A. M. and Borg L. E. (2014) A young solidification age for the lunar magma ocean. *Geochim. Cosmochim. Acta* **140**, 227–240.

Gagnepain-Beyneix J., Lognonné P., Chenet H., Lombardi D. and Spohn T. (2006) A seismic model of the lunar mantle and constraints on temperature and mineralogy. *Phys. Earth Planet. Int.* **159**, 140–166.

Garrick-Bethell I., Nimmo F. and Wieczorek M. A. (2010) Structure and formation of the lunar farside Highlands. *Science* **330**, 949–951.

Ghiorso M. S., Hirschmann M. M., Reiners P. W. and Kress, III, V. C. (2002) The pMELTS: a revision of MELTS for improved calculation of phase relations and major element partitioning related to partial melting of the mantle to 3 GPa. *Geochem. Geophys. Geosyst.* **3**, 1030.

Ghiorso M. S. and Sack R. O. (1995) Chemical mass transfer in magmatic processes IV. A revised and internally consistent thermodynamic model for the interpolation and extrapolation of liquid-solid equilibria in magmatic systems at elevated temperatures and pressures. *Contrib. Mineral. Petrol.* **119**, 197–212.

Glotch T. D., Hagerty J. J., Lucey P. G., Hawke B. R., Giguere T. A., Arnold J. A., Williams J.-P., Jolliff B. L. and Paige D. A. (2011) The Mairan domes: silicic volcanic constructs on the Moon. *Geophys. Res. Lett.* **38**, L21204.

Glotch T. D., Lucey P. G., Bandfield J. L., Greenhagen B. T., Thomas I. R., Elphic R. C., Bowles N., Wyatt M. B., Allen C.

C., Hanna K. D. and Paige D. A. (2010) Highly silicic compositions on the Moon. *Science* **329**, 1510–1513.
Gross J. and Treiman A. H. (2011) Unique spinel-rich lithology in lunar meteorite ALHA 81005: origin and possible connection to M3 observations of the farside highlands. *J. Geophys. Res. Planets* **116**, E10009.
Gross J., Treiman A. H. and Mercer C. N. (2014) Lunar feldspathic meteorites: constraints on the geology of the lunar highlands, and the origin of the lunar crust. *Earth Planet. Sci. Lett.* **388**, 318–328.
Grove T. L. and Bence A. E. (1979) Crystallization kinetics in a multiply saturated basalt magma – an experimental study of Luna 24 ferrobasalt. *Proc. Lunar Planet. Sci. Conf.* **10**, 439–478.
Hallis L. J., Anand M. and Strekopytov S. (2014) Trace-element modelling of mare basalt parental melts: implications for a heterogeneous lunar mantle. *Geochim. Cosmochim. Acta* **134**, 289–316.
Hart S. R. and Zindler A. (1986) In search of a bulk-Earth composition. *Chem. Geol.* **57**, 247–267.
Hartmann W. K. and Davis D. R. (1975) Satellite-sized planetesimals and lunar origin. *Icarus* **24**, 504–515.
Hays J. F. (1966) Lime-alumina-silica. *Carnegie Inst. Washington Year Book* **65**, 234–239.
Hess P. C. and Parmentier E. M. (1995) A model for the thermal and chemical evolution of the Moon's interior: implications for the onset of mare volcanism. *Earth Planet. Sci. Lett.* **134**, 501–514.
Hess P. C., Rutherford M. J., Guillemette R. N., Ryerson F. J. and Tuchfeld H. A. (1975) Residual products of fractional crystallization in lunar magmas: an experimental study. *Proc. Lunar Sci. Conf.* **6**, 895–909.
Hood L. L. and Jones J. H. (1987) Geophysical constraints on lunar bulk composition and structure: a reassessment. *J. Geophys. Res.* **92**, E396–E410.
Hui H., Neal C. R., Shih C. Y. and Nyquist L. E. (2013a) Petrogenetic association of the oldest lunar basalts: combined Rb-Sr isotopic and trace element constraints. *Earth Planet. Sci. Lett.* **373**, 150–159.
Hui H., Peslier A. H., Zhang Y. and Neal C. R. (2013b) Water in lunar anorthosites and evidence for a wet early Moon. *Nat. Geosci.* **6**, 177–180.
Ishihara Y., Goossens S., Matsumoto K., Noda H., Araki H., Namiki N., Hanada H., Iwata T., Tazawa S. and Sasaki S. (2009) Crustal thickness of the Moon: implications for farside basin structures. *Geophys. Res. Lett.* **36**, L19202.
Johannes W., Bell P. M., Mao H. K., Boettcher A. L., Chipman D. W., Hays J. F., Newton R. C. and Seifert F. (1971) An interlaboratory comparison of piston-cylinder pressure calibration using the albite-breakdown reaction. *Contrib. Mineral. Petrol.* **32**, 24–38.
Jolliff B. L., Floss C., McCallum I. S. and Schwartz J. M. (1999) Geochemistry, petrology, and cooling history of 14161,7373: a plutonic lunar sample with textural evidence of granitic-fraction separation by silicate-liquid immiscibility. *Am. Mineral.* **84**, 821–837.
Jolliff B. L., Gillis J. J., Haskin L. A., Korotev R. L. and Wieczorek M. A. (2000) Major lunar crustal terranes: surface expressions and crust-mantle origins. *J. Geophys. Res. Planets* **105**, 4197–4216.
Jolliff B. L., Wiseman S. A., Lawrence S. J., Tran T. N., Robinson M. S., Sato H., Hawke B. R., Scholten F., Oberst J., Hiesinger H., van der Bogert C. H., Greenhagen B. T., Glotch T. D. and Paige D. A. (2011) Non-mare silicic volcanism on the lunar farside at Compton-Belkovich. *Nat. Geosci.* **4**, 566–571.
Joy K. H., Crawford I. A., Downes H., Russell S. S. and Kearsley A. T. (2006) A petrological, mineralogical, and chemical analysis of the lunar mare basalt meteorite LaPaz Icefield 02205, 02224, and 02226. *Meteorit. Planet. Sci.* **41**, 1003–1025.
Jones J. H. and Delano J. W. (1989) A three-component model for the bulk composition of the Moon. *Geochim. Cosmochim. Acta* **53**, 513–527.
Khan A., Maclennan J., Taylor S. R. and Connolly J. A. D. (2006) Are the Earth and the Moon compositionally alike? Inferences on lunar composition and implications for lunar origin and evolution from geophysical modeling. *J. Geophys. Res.* **111**, E05005.
Khan A., Mosegaard K. and Rasmussen K. L. (2000) A new seismic velocity model for the Moon from a Monte Carlo inversion of the Apollo lunar seismic data. *Geophys. Res. Lett.* **27**, 1591–1594.
Khan A., Pommier A., Neumann G. A. and Mosegaard K. (2013) The lunar moho and the internal structure of the Moon: a geophysical perspective. *Tectonophysics* **609**, 331–352.
Kirk R. L. and Stevenson D. J. (1989) The competition between thermal contraction and differentiation in the stress history of the Moon. *J. Geophys. Res.* **94**, 12133–12144.
Kleine T., Palme H., Mezger M. and Halliday A. N. (2005) Hf-W chronometry of lunar metals and the age and early differentiation of the Moon. *Science* **310**, 1671–1674.
Korotev R. L., Jolliff B. L., Zeigler R. A., Gillis J. J. and Haskin L. A. (2003) Feldspathic lunar meteorites and their implications for compositional remote sensing of the lunar surface and the composition of the lunar crust. *Geochim. Cosmochim. Acta* **67**, 4895–4923.
Lin Y., Tronche E. J., Steenstra E. S. and van Westrenen W. (2016) Evidence for an early wet Moon from experimental crystallization of the lunar magma ocean. *Nat. Geosci.* **10**, 14–18.
Lin Y., Tronche E. J., Steenstra E. S. and van Westrenen W. (2017) Experimental constraints on the solidification of a nominally dry lunar magma ocean. *Earth Planet. Sci. Lett.* **471**, 104–116.
Lindsley D. H. and Munoz J. L. (1969) Subsolidus relations along the join hedenbergite-ferrosilite. *Am. J. Sci.* **267-A**, 295–324.
Lognonné P. (2005) Planetary seismology. *Ann. Rev. Earth Planet. Sci.* **33**, 571–604.
Lognonné P. and Johnson C. (2007) 10.03 – planetary seismology. In *Treatise on Geophysics* (ed. G. Schubert). Elsevier, Amsterdam, pp. 69–122.
Longhi J. (1977) Magma oceanography 2: chemical evolution and crustal formation. *Proc. Lunar Sci. Conf.* **8**, 601–621.
Longhi J. (1980) A model of early lunar differentiation. *Proc. Lunar Planet. Sci. Conf.* **11**, 289–315.
Longhi J. (1981) Preliminary modeling of high pressure partial melting: implications for early lunar differentiation. *Proc. Lunar Planet. Sci. Conf.* **12**, 1001–1018.
Longhi J. (2003) A new view of lunar ferroan anorthosites: postmagma ocean petrogenesis. *J. Geophys. Res. Planets* **108**, E8.
Longhi J. (2006) Petrogenesis of picritic mare magmas: constraints on the extent of early lunar differentiation. *Geochim. Cosmochim. Acta* **70**, 5919–5934.
Longhi J. and Ashwal L. D. (1985) Two-stage models for lunar and terrestrial anorthosites: petrogenesis without a magma ocean. *J. Geophys. Res.* **90**(Supplement), C571–C584.
Longhi J., Durand S. R. and Walker D. (2010) The pattern of Ni and Co abundances in lunar olivines. *Geochim. Cosmochim. Acta* **74**, 784–798.
McCubbin F. M., Vander Kaaden K. E., Tartèse R., Klima R. L., Liu Y., Mortimer J., Barnes J. J., Shearer C. K., Treiman A. H., Lawrence D. J., Elardo S. M., Hurley D. M., Boyce J. W. and Anand M. (2015) Magmatic volatiles (H, C, N, F, S, Cl) in the lunar mantle, crust, and regolith: abundances, distributions, processes, and reservoirs. *Am. Mineral.* **100**, 1668–1707.

McDonough W. F. and Sun S.-S. (1995) The composition of the Earth. *Chem. Geol.* **120**, 223–253.

Médard E., McCammon C. A., Barr J. A. and Grove T. L. (2008) Oxygen fugacity, temperature reproducibility, and H2O contents of nominally anhydrous piston-cylinder experiments using graphite capsules. *Am. Mineral.* **93**, 1838–1844.

Melosh H. J., Kendall J., Horgan B., Johnson B. C., Bowling T., Lucey P. G. and Taylor G. J. (2017) South Pole-Aitken basin ejecta reveal the Moon's upper mantle. *Geology* **45**, 1063–1066.

Mueller S., Taylor G. J. and Phillips R. J. (1988) Lunar composition: a geophysical and petrological synthesis. *J. Geophys. Res. Solid Earth* **93**, 6338–6352.

Münker C. (2010) A high field strength element perspective on early lunar differentiation. *Geochim. Cosmochim. Acta* **74**, 7340–7361.

Nakamura Y. (1983) Seismic velocity structure of the lunar mantle. *J. Geophys. Res.* **88**, 677–686.

Namur O., Charlier B., Pirard C., Hermann J., Liégeois J.-P. and Vander Auwera J. (2011) Anorthosite formation by plagioclase flotation in ferrobasalt and implications for the lunar crust. *Geochim. Cosmochim. Acta* **75**, 4998–5018.

Neal C. R. (2001) Interior of the Moon: the presence of garnet in the primitive deep lunar mantle. *J. Geophys. Res. Planets* **106**, 27865–27885.

Nemchin A., Timms N., Pidgeon R., Geisler T., Reddy S. and Meyer C. (2009) Timing of crystallization of the lunar magma ocean constrained by the oldest zircon. *Nat. Geosci.* **2**, 133–136.

O'Neill H. S. C. (1991) The origin of the Moon and the early history of the earth—a chemical model. Part 1: The Moon. *Geochim. Cosmochim. Acta* **55**, 1135–1157.

Ohtake M., Matsunaga T., Haruyama J., Yokota Y., Morota T., Honda C., Ogawa Y., Torii M., Miyamoto H., Arai T., Hirata N., Iwasaki A., Nakamura R., Hiroi T., Sugihara T., Takeda H., Otake H., Pieters C. M., Saiki K., Kitazato K., Abe M., Asada N., Demura H., Yamaguchi Y., Sasaki S., Kodama S., Terazono J., Shirao M., Yamaji A., Minami S., Akiyama H. and Josset J.-L. (2009) The global distribution of pure anorthosite on the Moon. *Nature* **461**, 236–240.

Ohtake M., Takeda H., Matsunaga T., Yokota Y., Haruyama J., Morota T., Yamamoto S., Ogawa Y., Hiroi T., Karouji Y., Saiki K. and Lucey P. G. (2012) Asymmetric crustal growth on the Moon indicated by primitive farside highland materials. *Nat. Geosci.* **5**, 384–388.

Pieters C. M., Besse S., Boardman J., Buratti B., Cheek L., Clark R. N., Combe J. P., Dhingra D., Goswami J. N., Green R. O., Head J. W., Isaacson P., Klima R., Kramer G., Lundeen S., Malaret E., McCord T., Mustard J., Nettles J., Petro N., Runyon C., Staid M., Sunshine J., Taylor L. A., Thaisen K., Tompkins S. and Whitten J. (2011) Mg-spinel lithology: a new rock type on the lunar farside. *J. Geophys. Res. Planets* **116**, E00G08.

Philpotts A. R., Shi J. and Brustman C. (1998) Role of plagioclase crystal chains in the differentiation of partly crystallized basaltic magma. *Nature* **395**, 343–346.

Prissel T. C., Parman S. W., Jackson C. R. M., Rutherford M. J., Hess P. C., Head J. W., Cheek L., Dhingra D. and Pieters C. M. (2014) Pink Moon: the petrogenesis of pink spinel anorthosites and implications concerning Mg-suite magmatism. *Earth Planet. Sci. Lett.* **403**, 144–156.

Rai N. and van Westrenen W. (2014) Lunar core formation: new constraints from metal–silicate partitioning of siderophile elements. *Earth Planet. Sci. Lett.* **388**, 343–352.

Russell S. S., Joy K. H., Jeffries T. E., Consolmagno G. J. and Kearsley A. (2014) Heterogeneity in lunar anorthosite meteorites: implications for the lunar magma ocean model. *Philos. Trans. R. Soc. Lond. Ser. A Math. Phys. Eng. Sci.* **372**, 20130241.

Rutherford M. J., Hess P. C., Ryerson F. J., Campbell H. W. and Dick P. A. (1976) The chemistry, origin and petrogenetic implications of lunar granite and monzonite. *Proc. Lunar Sci. Conf.* **7**, 1723–1740.

Saal A. E., Hauri E. H., Cascio M. L., Van Orman J. A., Rutherford M. C. and Cooper R. F. (2008) Volatile content of lunar volcanic glasses and the presence of water in the Moon/'s interior. *Nature* **454**, 192–195.

Sack R. O. and Ghiorso M. S. (1994) Thermodynamics of multicomponent pyroxenes: II. Phase relations in the quadrilateral. *Contrib. Mineral. Petrol.* **116**, 287–300.

Sato M., Hickling N. L. and McLane J. E. (1973) Oxygen fugacity values of Apollo 12, 14, and 15 lunar samples and reduced state of lunar magmas. *Proc. Lunar Sci. Conf.* **4**, 1061–1079.

Schmidt M. W., Forien M., Solferino G. and Bagdassarov N. (2012) Settling and compaction of olivine in basaltic magmas: an experimental study on the time scales of cumulate formation. *Contrib. Mineral. Petrol.* **164**, 959–976.

Seddio S. M., Jolliff B. L., Korotev R. L. and Zeigler R. A. (2013) Petrology and geochemistry of lunar granite 12032,366–19 and implications for lunar granite petrogenesis. *Am. Mineral.* **98**, 1697–1713.

Sharp Z. D., Shearer C. K., McKeegan K. D., Barnes J. D. and Wang Y. Q. (2010) The chlorine isotope composition of the Moon and implications for an anhydrous mantle. *Science* **329**, 1050–1053.

Shearer C. K., Hess P. C., Wieczorek M. A., Pritchard M. E., Parmentier E. M., Borg L. E., Longhi J., Elkins-Tanton L. T., Neal C. R., Antonenko I., Canup R. M., Halliday A. N., Grove T. L., Hager B. H., Lee D.-C. and Wiechert U. (2006) Thermal and magmatic evolution of the Moon. *Rev. Mineral. Geochem.* **60**, 365–518.

Sisson T. W. and Grove T. L. (1993) Experimental investigations of the role of H2O in calc-alkaline differentiation and subduction zone magmatism. *Contrib. Mineral. Petrol.* **113**, 143–166.

Smith J. V., Anderson A. T., Newton R. C., Olsen E. J., Wyllie P. J., Crewe A. V., Isaacson M. S. and Johnson D. (1970) Petrologic history of the Moon inferred from petrography, mineralogy and petrogenesis of Apollo 11 rocks. *Proc. Apollo 11 Lunar Sci. Conf.* **1**, 897–925.

Snyder G. A., Taylor L. A. and Neal C. R. (1992) A chemical model for generating the sources of mare basalts: combined equilibrium and fractional crystallization of the lunar magmasphere. *Geochim. Cosmochim. Acta* **56**, 3809–3823.

Solomon S. C. (1980) Differentiation of crusts and cores of the terrestrial planets: lessons for the early Earth? *Precambr. Res.* **10**, 177–194.

Solomon S. C. and Chaiken J. (1976) Thermal expansion and thermal stress in the Moon and terrestrial planets: clues to early thermal history. *Proc. Lunar Sci. Conf.* **7**, 3229–3243.

Solomon S. C. and Longhi J. (1977) Magma oceanography: 1. Thermal evolution. *Proc. Lunar Sci. Conf.* **8**, 583–599.

Steenstra E. S., Rai N., Knibbe J. S., Lin Y. H. and van Westrenen W. (2016) New geochemical models of core formation in the Moon from metal–silicate partitioning of 15 siderophile elements. *Earth Planet. Sci. Lett.* **441**, 1–9.

Stevenson D. J. (1987) Origin of the Moon-The collision hypothesis. *Ann. Rev. Earth Planet. Sci.* **15**, 271–315.

Suckale J., Elkins-Tanton L. T. and Sethian J. A. (2012) Crystals stirred up: 2. Numerical insights into the formation of the earliest crust on the Moon. *J. Geophys. Res. Planets* **117**, E08005.

Sun Y., Li L. and Zhang Y. (2017) Detection of Mg-spinel bearing central peaks using M3 images: implications for the petrogenesis of Mg-spinel. *Earth Planet. Sci. Lett.* **465**, 48–58.

Takeda H., Yamaguchi A., Bogard D. D., Karouji Y., Ebihara M., Ohtake M., Saiki K. and Arai T. (2006) Magnesian anorthosites and a deep crustal rock from the farside crust of the Moon. *Earth Planet. Sci. Lett.* **247**, 171–184.

Taylor D. J., McKeegan K. D. and Harrison T. M. (2009) Lu-Hf zircon evidence for rapid lunar differentiation. *Earth Planet. Sci. Lett.* **279**, 157–164.

Taylor G. J. and Wieczorek M. A. (2014) Lunar bulk chemical composition: a post-Gravity Recovery and Interior Laboratory reassessment. *Philos. Trans. R. Soc. Lond. Ser. A Math. Phys. Eng. Sci.* **372**, 20130242.

Taylor S. R. (1982) *Planetary Science: A Lunar Perspective*. Lunar and Planetary Institute, Houston, p. 502.

Taylor S. R. and Bence A. E. (1975) Evolution of the lunar highland crust. *Proc. Lunar Sci. Conf.* **6**, 1121–1141.

Taylor S. R., Taylor G. J. and Taylor L. A. (2006) The Moon: a Taylor perspective. *Geochim. Cosmochim. Acta* **70**, 5904–5918.

Tonks W. B. and Melosh H. J. (1993) Magma ocean formation due to giant impacts. *J. Geophys. Res.* **98**, 5319–5333.

Touboul M., Kleine T., Bourdon B., Palme H. and Wieler R. (2007) Late formation and prolonged differentiation of the Moon inferred from W isotopes in lunar metals. *Nature* **450**, 1206–1209.

Touboul M., Kleine T., Bourdon B., Palme H. and Wieler R. (2009) Tungsten isotopes in ferroan anorthosites: implications for the age of the Moon and lifetime of its magma ocean. *Icarus* **199**, 245–249.

Walker D., Longhi J. and Hays J. F. (1975) Differentiation of a very thick magma body and implications for the source regions of mare basalts. *Proc. Lunar Sci. Conf.* **6**, 1103–1120.

Wänke H. and Dreibus G. (1982) Chemical and isotopic evidence for the early history of the Earth-Moon system. In *Tidal Friction and the Earth's Rotation II* (eds. P. Brosche and J. Sündermann). Springer-Verlag, Berlin, pp. 322–344.

Warren P. H. (1985) The magma ocean concept and lunar evolution. *Ann. Rev. Earth Planet. Sci.* **13**, 201–240.

Warren P. H. (1990) Lunar anorthosites and the magma-ocean plagioclase-flotation hypothesis; importance of FeO enrichment in the parent magma. *Am. Mineral.* **75**, 46–58.

Warren P. H. (2005) "New" lunar meteorites: implications for composition of the global lunar surface, lunar crust, and the bulk Moon. *Meteorit. Planet. Sci.* **40**, 477–506.

Warren P. H., Taylor G. J., Keil K., Shirley D. N. and Wasson J. T. (1983) Petrology and chemistry of two "large" granite clasts from the Moon. *Earth Planet. Sci. Lett.* **64**, 175–185.

Warren P. H. and Wasson J. T. (1979a) Effects of pressure on the crystallization of a "chondritic" magma ocean and implications for the bulk composition of the Moon. *Proc. Lunar Planet. Sci. Conf.* **10**, 2051–2083.

Warren P. H. and Wasson J. T. (1979b) Origin of KREEP. *Rev. Geophys. Space Phys.* **17**, 73–88.

Watters T. R., Robinson M. S., Banks M. E., Tran T. and Denevi B. W. (2012) Recent extensional tectonics on the Moon revealed by the Lunar Reconnaissance Orbiter Camera. *Nat. Geosci.* **5**, 181–185.

Wiechert U., Halliday A. N., Lee D.-C., Snyder G. A., Taylor L. A. and Rumble D. (2001) Oxygen isotopes and the Moon-forming giant impact. *Science* **294**, 345–348.

Wieczorek M. A., Jolliff B. L., Khan A., Pritchard M. E., Weiss B. P., Williams J. G., Hood L. L., Righter K., Neal C. R., Shearer C. K., McCallum I. S., Tompkins S., Hawke B. R., Peterson C., Gillis J. J. and Bussey B. (2006) The constitution and structure of the lunar interior. *Rev. Mineral. Geochem.* **60**, 221–364.

Wieczorek M. A., Neumann G. A., Nimmo F., Kiefer W. S., Taylor G. J., Melosh H. J., Phillips R. J., Solomon S. C., Andrews-Hanna J. C., Asmar S. W., Konopliv A. S., Lemoine F. G., Smith D. E., Watkins M. M., Williams J. G. and Zuber M. T. (2013) The crust of the Moon as seen by GRAIL. *Science* **339**, 671–675.

Wood J. A., Dickey J. S., Marvin U. B. and Powell B. N. (1970) Lunar anorthosites and a geophysical model of the Moon. *Proc. Lunar Sci. Conf.* **1**, 965–988.

Zhang J., Dauphas N., Davis A. M., Leya I. and Fedkin A. (2012) The proto-Earth as a significant source of lunar material. *Nat. Geosci.* **5**, 251–255.

Zuber M. T., Smith D. E., Lemoine F. G. and Neumann G. A. (1994) The shape and internal structure of the Moon from the Clementine mission. *Science* **266**, 1839–1843.

Associate editor: Rajdeep Dasgupta